UNIVERSIDADE FEDERAL DO CEARÁ
CENTRO DE TECNOLOGIA
DEPARTAMENTO DE ENGENHARIA DE TELEINFORMÁTICA
PROGRAMA DE PÓS-GRADUAÇÃO EM ENGENHARIA DE TELEINFORMÁTICA

EZEQUIAS MÁRCIO SILVA DE SANTANA JÚNIOR

OPTIMIZATION AND NETWORK PERFORMANCE EVALUATION OF BEAMFORMING AND DYNAMIC DTX TECHNIQUES IN 5G/6G SYSTEMS

FORTALEZA
2022

EZEQUIAS MÁRCIO SILVA DE SANTANA JÚNIOR

OPTIMIZATION AND NETWORK PERFORMANCE EVALUATION OF BEAMFORMING AND DYNAMIC DTX TECHNIQUES IN 5G/6G SYSTEMS

Dissertação apresentada ao Curso de Mestrado em Engenharia de Teleinformática da Universidade Federal do Ceará, como parte dos requisitos para obtenção do Título de Mestre em Engenharia de Teleinformática. Área de concentração: Sinais e Sistemas

Orientador: Prof. Dr.-Ing. Yuri Carvalho Barbosa Silva

Coorientador: Prof. Dr. Igor Moaco Guerreiro

FORTALEZA
2022

Dados Internacionais de Catalogação na Publicação
Universidade Federal do Ceará
Biblioteca Universitária
Gerada automaticamente pelo módulo Catalog, mediante os dados fornecidos pelo(a) autor(a)

S223o Santana Júnior, Ezequias Márcio Silva de.
Optimization and network performance evaluation of beamforming and dynamic DTX techniques in 5G/6G systems / Ezequias Márcio Silva de Santana Júnior. – 2022.
55 f. : il. color.

Dissertação (mestrado) – Universidade Federal do Ceará, Centro de Tecnologia, Programa de Pós-Graduação em Engenharia de Teleinformática, Fortaleza, 2022.
Orientação: Prof. Dr. Yuri Carvalho Barbosa Silva.
Coorientação: Prof. Dr. Igor Moaco Guerreiro.

1. Bandas sub-terahertz. 2. Transmissão descontinuada. 3. Superaquecimento. 4. Aprendizado profundo. 5. Formatação de feixes. I. Título.

CDD 621.38

EZEQUIAS MÁRCIO SILVA DE SANTANA JÚNIOR

OPTIMIZATION AND NETWORK PERFORMANCE EVALUATION OF BEAMFORMING AND DYNAMIC DTX TECHNIQUES IN 5G/6G SYSTEMS

Dissertação apresentada ao Curso de Mestrado em Engenharia de Teleinformática da Universidade Federal do Ceará, como parte dos requisitos para obtenção do Título de Mestre em Engenharia de Teleinformática. Área de concentração: Sinais e Sistemas

Aprovado em: 01/08/2022.

BANCA EXAMINADORA

Prof. Dr.-Ing. Yuri Carvalho Barbosa Silva (Orientador)
Universidade Federal do Ceará

Prof. Dr. Igor Moaco Guerreiro (Coorientador)
Universidade Federal do Ceará

Prof. Dr. Leonardo Aguayo
Universidade de Brasília

Prof. Dr.-Ing. Tarcisio Ferreira Maciel
Universidade Federal do Ceará

For my family.

AGRADECIMENTOS

Gostaria de agradecer primeiramente à minha família por todo o incentivo e apoio durante toda a minha jornada acadêmica, em especial à minha avó Ivanilda por todo amor, carinho e cuidados. Aos meus pais, Suzana e Ezequias, e à minha tia Mônica por sempre acreditarem em mim. Agradeço à minha namorada Thaís pelo amor, carinho e por estar sempre ao meu lado em todos os momentos. Também gostaria de agradecer a todos os meus professores por todo conhecimento e conselhos passados. Sou muito grato ao Prof. Yuri por me acompanhar desde a graduação e por todo o mestrado como meu orientador. Agradeço também ao meu coorientador, Prof. Igor Guerreiro, por todo o acompanhamento durante o mestrado e no projeto de pesquisa, o qual foi um momento onde pude aprender bastante. Gostaria de agradecer a todos os membros do Grupo de Pesquisa em Telecomunicações Sem-fio (GTEL) da Universidade Federal do Ceará (UFC) pelas experiências profissionais que adquiri como pesquisador. Agradeço aos meus colegas de projeto (Lászlon, Carlos e Michel) por todas as discussões e ajuda no desenvolvimento do meu tema de pesquisa. Finalmente, gostaria de agradecer ao apoio da Ericsson Research (contrato de cooperação técnico-científica UFC.49) e da Coordenacão de Aperfeiçoamento de Pessoal de Nivel Superior – Brasil (CAPES) pelo apoio técnico e financeiro ao longo do desenvolvimento do meu mestrado.

RESUMO

A fim de apoiar a evolução dos sistemas de comunicações celulares para além da quinta geração (5G), tem sido considerada pela indústria e pela academia a otimização e o desenvolvimento de novas tecnologias de comunicação como a comunicação de múltiplas entradas e múltiplas saídas (MIMO) massiva e a exploração de um maior espectro de frequência usando faixas de frequência em ondas milimétricas (mmWave) e terahertz (THz). No entanto, alguns desafios surgem durante a aplicação dessas técnicas nesses novos cenários. Neste contexto, esta dissertação aborda dois cenários diferentes de sistemas de comunicação móvel, cada um considerando um problema específico em relação aos sistemas 5G e de sexta geração (6G). Primeiramente, é abordado o problema de beamforming robusto em sistemas multiusuários de múltiplas entradas e saídas únicas (MU-MISO). Para tanto, avaliou-se o desempenho de uma estratégia de formatação de feixes baseada em redes neurais profundas (DNN) sob condições imperfeitas de canal. Uma análise de robustez foi fornecida adicionando controladamente um termo de ruído aditivo independente ao canal. A estratégia de formatação de feixe baseada em DNN é comparada com a solução clássica de erro quadrado médio ponderado mínimo (WMMSE) em termos do impacto da informação de estado de canal imperfeita (ICSI) na soma da taxa média alcançada pelos usuários. Resultados mostraram que a estratégia baseada em DNN é viável em termos de complexidade computacional e tão robusta quanto a solução iterativa do WMMSE. Na segunda parte, é avaliado o desempenho da rede de um sistema celular operando a 100 GHz com largura de banda em torno de 3 GHz sob um regime de dinâmico de transmissão descontinuada (DTX) aplicado aos pontos de transmissão e recepção (TRP). O uso de faixas de frequência na ordem de THz é considerado como um meio para alcançar taxas de dados mais altas em sistemas 6G. Adicionalmente, para lidar com condições de propagação mais severas em faixas de THz, foi adotada uma rede com múltiplos TRP equipados com grandes arranjos de antenas que promovem conexão a equipamentos de usuário (UEs) equipados com múltiplos painéis. Para evitar problemas de superaquecimento, foi proposto um método de DTX do lado do TRP, que controla as transmissões de *downlink* enquanto garante o envio de sinais de referência específicos da célula. Resultados de simulação considerando diferentes configurações de DTX e cargas de tráfego foram apresentados e discutidos. Os resultados mostraram que o sistema THz considerado com o método DTX proposto pode fornecer taxas de dados mais altas em comparação com um sistema mmWave padrão operando a 28 GHz, promovendo um ganho de taxa de dados 6.84 vezes maior.

Palavras-chave: aprendizado profundo; MU-MISO; WMMSE; formatação e gerenciamento de feixes; bandas sub-THz; superaquecimento; transmissão descontinuada.

ABSTRACT

In order to support the evolution of cellular communication systems towards the fifth generation (5G) and beyond, the industry and the research community have considered the optimization and development of communication technologies, such as massive multiple-input multiple-output (MIMO) and the exploration of a larger frequency spectrum using millimiter wave (mmWave) and terahertz (THz) bands. However, some challenges emerge during the application of these techniques in these new scenarios. In this context, this dissertation addresses two different scenarios of mobile communication systems, each considering one specific problem regarding 5G and 6G systems. First, it addresses the problem of robust beamforming in multi-user multiple-input single-output (MU-MISO) systems. To this end, it assesses the performance of a deep neural network (DNN)-based beamforming strategy under imperfect channel conditions. A robustness analysis has been provided by adding a controlled independent additive noise term to the channel. The DNN-based beamforming strategy is compared with the classical weighted minimum mean square error (WMMSE) solution in terms of the impact of imperfect channel state information (ICSI) on the average sum rate. Results have shown that the deep neural network (DNN)-based strategy is viable in terms of complexity and is as robust as the weighted minimum mean square error (WMMSE). In the second part, it evaluates the network performance of a cellular system operating at 100 GHz with bandwidth of around 3 GHz under a dynamic transmission and reception point (TRP)-side discontinuous transmission (DTX) regime. The use of THz bands are envisioned as a means to achieve higher data rates in sixth generation (6G) systems. Additionally, to deal with more severe propagation conditions in THz bands, a network with multiple TRPs equipped with large antenna arrays serving multi-panel user equipment (UE) has been adopted. To avoid overheating issues, a TRP-side DTX method has been proposed, which controls downlink transmissions while guaranteeing cell-specific reference signaling. Simulation results considering different DTX settings and traffic loads have been presented and discussed. Results have shown that the considered THz system with the proposed DTX method can provide higher data rates in comparison with a typical, baseline (mmWave) system operating at 28 GHz. It was possible to reach at least 6.84 times higher data rates.

Keywords: deep learning; MU-MISO; WMMSE; deamforming and beam management; sub-THz bands; TRP panel overheating; siscontinuous transmission.

LIST OF FIGURES

LIST OF TABLES

LIST OF ABBREVIATIONS AND ACRONYMS

2G	second generation
3G	third generation
3GPP	3rd generation partnership project
4G	fourth generation
5G	fifth generation
5G-StoRM	5G stochastic radio channel for dual mobility
6G	sixth generation
AD	analog-to-digital
BBU	baseband unit
BF	beamforming
BLER	block error rate
BM	beam management
BPL	beam pair link
BS	base station
CDF	cumulative distribution function
CDMA	code division multiple access
CSI	channel state information
DA	digital-to-analog
DFT	discrete Fourier transform
DL	downlink
DNN	deep neural network
DPBF	dual polarized beamforming
DRX	discontinuous reception
DTX	discontinuous transmission
eMBB	enhanced mobile broadband
FR2	frequency range 2
GSM	global system for mobile communication
HBF	hybrid beamforming
ICSI	imperfect channel state information
IoT	Internet of things
ISD	intersite distance
JT	joint transmission
KKT	Karush–Kuhn–Tucker
KPI	key performance indicator
LOS	line-of-sight
LTE	long term evolution

LTE-A	long term evolution advanced
MCS	modulation and coding scheme
MIMO	multiple-input multiple-output
mMTC	massive machine-type communication
mmWave	millimeter wave
MSE	mean square error
MU-MISO	multi-user multiple-input single-output
NC	non-coherent
NR	new radio
O2O	outdoor-to-outdoor
OFDM	orthogonal frequency division multiplexing
OFDMA	orthogonal frequency division multiple access
P1	procedure 1
P2	procedure 2
P3	procedure 3
PRB	physical resource block
RB	resource block
ReLU	rectified linear unit
RF	radio frequency
RS	reference signal
RSRP	reference signal received power
RZF	regularized zero-forcing
SINR	signal-to-interference-plus-noise ratio
SNR	signal-to-noise ratio
SS	synchronization signal
TDM	time division multiplex
THz	terahertz
TRP	transmission and reception point
TTI	transmit time interval
UE	user equipment
UMi	urban micro
URA	uniform rectangular array
URLLC	ultra-reliable and low-latency communication
WMMSE	weighted minimum mean square error
WSR	weighted sum rate
ZF	zero-forcing

LIST OF SYMBOLS

$(\cdot)^*$	Complex conjugate operator
$(\cdot)^H$	Complex conjugate tranpose operator
B_υ	Number of bits that modulation and coding scheme (MCS) υ can transmit in a single resource block (RB)
$B_{k,b}$	Number of received bits at the b-th panel of user equipment (UE) k
K^{cool}	Number of slots needed for a transmission and reception point (TRP) to cool down
K	Number of UEs
L^{P1}	Number of wide beams used for procedure 1 (P1)
L^{P2}	Number of narrow beams used for procedure 2 (P2)
L^{P3}	Number of narrow beams used for procedure 3 (P3)
L^{SS}	Number of transmitted cell-specific synchronization signals (SSs)
L_{BW}	System bandwidth
L_{sc}	Subcarrier spacing
M	Number of base station (BS) antenna elements
N_r	Number of cross-pole elements of each UE panel
N_t	Number of cross-pole elements of the TRP panel
N_{RB}	Number of RBs
N_{slot}	Number of slots per subframe
P_{TX}	TRP transmit power
$P_{\max}$	Downlink transmit power constraint
R_k^{buffer}	Number of bits in the transmitter buffer for UE k
R_{pkt}	Length in bits of the generated packets
$T^{\text{CSI-RS}}$	Channel state information (CSI)-reference signals (RSs) period
T^{SS}	SSs transmission period
T_{pkt}	Packet generation period
$\mathcal{S}_m$	Set of all the UE panel candidates to be scheduled
α_k	Constant system weight for the k-th UE
$\bar{\gamma}_{k,b,m}$	Estimated signal-to-interference-plus-noise ratio (SINR) at the b-th panel of UE k
γ_k	SINR at receiver k
$\gamma_{k,b,m}$	SINR at the b-th panel of UE k
$\hat{\boldsymbol{\lambda}}$	Predicted weight vector
$\hat{\mathbf{h}}_k$	Imperfect channel response of the k-th UE available at the BS
$\hat{\mathbf{p}}$	Predicted power coefficient vector
$\mathbb{E}\{\cdot\}$	Expected value operator

$\mathbf{I}_M$	Identity matrix of dimension $M \times M$
$\mathbf{U}$	Diagonal matrix containing the users' mean square error (MSE) filter coefficients
$\mathbf{V}$	Diagonal matrix containing the users' weighted minimum mean square error (WMMSE) weights
$\mathbf{W}$	Downlink beamforming matrix
$\mathbf{h}_e$	Independent fast fading error
$\mathbf{h}_k$	Channel vector between the BS and the k-th UE
$\mathbf{h}$	Vector of the stacked channel coefficients between the BS and all UEs
$\mathbf{w}_k$	Beamforming vector for the k-th UE
$\mathcal{A}_{N_r,1}$	Set of UE wide beams
$\mathcal{A}_{N_t,2}$	Set of TRP wide beams
$\mathcal{B}_{N_r,1}$	Set of UE narrow receive beams
$\mathcal{B}_{N_t,2}$	Set of TRP narrow beams
$\mathcal{D}_{N_r,1}$	Set of all column vectors of an $N_r \times N_r$ discrete Fourier transform (DFT) matrix with oversampling factor of 1
$\mathcal{D}_{N_t,2}$	Set of column vectors of an $N_t \times 2N_t$ DFT matrix with oversampling factor of 2
$\mathcal{M}$	TRP set
$\mathcal{Q}_{\mathrm{RS}}$	Set of RBs used for reference signal transmissions
$\mathcal{Q}$	RB set
$\mathcal{S}_j^{\mathrm{data}}$	Subset of orthogonal frequency division multiplexing (OFDM) symbols of slot j that convey data
$\mathbf{w}_k^\star$	Optimal beamforming vector for the k-th UE
$\mathbf{H}_{m,k,b}$	Dual-polarization channel matrix in the frequency domain
$\psi_{k,b,m}$	reference signal received power (RSRP) of the received signal at the b-th panel of UE k from TRP m
$\mathrm{Tr}(\cdot)$	Matrix trace operator
θ	Accuracy measure of the channel estimation process
$\tilde{\mathbf{h}}_k$	Channel fast fading component vector between the BS and the k-th UE
$\tilde{\mathbf{w}}_k$	Normalized beamforming vector for the k-th UE
$\tilde{\mathcal{M}}$	Set of available TRPs
$\tilde{\mathbf{H}}_{m,k,b}^{(\alpha,\beta)}$	Matrix of channel coefficients between the antenna elements of the m-th TRP and the b-th panel of the k-th UE per polarization pair (α, β)
$\mathbf{f}_m$	Dual-polarization beam of the TRP m
$\mathbf{w}_{k,b}$	Dual-polarization beam of the b-th panel of UE k
f_c	Carrier frequency
g_k	Channel large-scale fading gain between the BS and the k-th UE

$h_{m,k,b}$	Equivalent channel response between the TRP m and the b-th panel of UE k
n^{SS}	Number of consecutive slots conveying SSs
n_m^{slot}	Discontinuous transmission (DTX) slot counter of TRP m
n^{max}	DTX maximum slot counter threshold
n_m^{off}	DTX back-off period
n_m^{budget}	Slot budget for TRP m to transmit SSs
$r_{k,j}$	Achieved throughput of each UE k at slot j
s_m	Single multiple-input multiple-output (MIMO) stream transmitted symbols from TRPs
t_{slot}	Slot duration in seconds
u_k	MSE filter coefficient of the k-th UE
$u_{m,k,b}$	Scheduler fairness utility
v_k	WMMSE weight of the k-th UE
$\|\|\cdot\|\|_1$	ℓ_1 norm operator.

SUMMARY

1 INTRODUCTION

Over the past five decades the wireless mobile communication systems have evolved through five generations. The evolution of wireless communication technologies throughout the generations was driven by several factors as a result of their high diffusion and acceptance, alongside the new applications and services that can be provided.

The constant growth in the number of users, as well as the increase of the demand for wireless services with high mobility and capacity motivated the establishment of new use cases, scenarios, and requirements to be satisfied when evolving from one generation to the next.

The first generation of mobile communications was based on analog cellular systems and provided mobile telephony for the first time. Second generation (2G) systems introduced digital transmission technologies, enabling better signal processing capabilities and new data services, being the global system for mobile communication (GSM) the main standard for 2G [1]. The transition to modern mobile communication systems was introduced by the third generation (3G), providing high quality mobile boardband through fast Internet connection by exploiting new radio access technologies based on code division multiple access (CDMA). With the fourth generation (4G) of wireless communication systems, the LTE standard extended the mobile broadband services, providing higher data rates and supporting more users with less delay powered by orthogonal frequency division multiple access (OFDMA) in combination with the employment of multiple-input multiple-output (MIMO) systems.

The fifth generation (5G) systems are currently in the implementation stage across the world. 5G systems seek to provide reliable connectivity at any time in the most diverse scenarios [2], offering low latency, high transmission rates and high mobility, even in denser networks where a high demand for data per user is present, outperforming previous generations and increasing the number of potential applications of mobile systems. The target requirements envisioned to be met by 5G new radio (NR) standard in order to improve and extend LTE systems capabilities are depicted in the following three main use cases:

1. Enhanced mobile broadband (eMBB): This use case addresses the user centric applications, representing the direct evolution of 4G mobile boardband providing better QoS, enhanced user experience, and large data traffic by supporting even higher data rates.

2. Ultra-reliable and low-latency communication (URLLC): This use case extends previous generation systems by focusing on enabling mission critical connectivity for applications that require extremely high reliability and very low latency, such as real time services, autonomous vehicles, and automation in Industry 4.0.

3. Massive machine-type communication (mMTC): This use case focuses on providing and supporting dense connectivity to a large number of low-cost narrow-bandwidth

devices, prioritizing operation whit high energy efficiency. This scenario is the key enabler for Internet of things (IoT) applications.

In order to satisfy the requirements for 5G NR and promote its evolution toward beyond 5G and sixth generation (6G), the industry and the research community have considered the optimization and development of communications technologies regarding three different aspects: more advanced multi-antenna technologies, such as massive MIMO; exploration of higher frequency bands, e.g., millimeter wave (mmWave) bands to provide end users high data rates; and the employment of dense and heterogenous networks via small cells architecture.

1.1 Contributions and organization

In the context of the evolution and optimization of mobile wireless systems, this dissertation addresses two different scenarios of mobile communication systems, each considering one specific problem regarding aspects of 5G and 6G systems discussed in two self contained chapters.

The first scenario discussed in **Chapter 2** is in the context of optimization strategies for downlink transmissions and machine learning for communication systems. It addresses the problem of robust beamforming in multi-user multiple-input single-output (MU-MISO) systems, considering the performance of a deep neural network (DNN)-based beamforming strategy under imperfect channel state information (ICSI) conditions. It also provides a robustness analysis in the presence of a controlled additive error term in the fast fading component of the channel.

The second scenario is discussed in **Chapter 3** and considers the context of exploiting higher operation frequencies for beyond 5G systems and their impact on the network performance under a dynamic discontinuous transmission (DTX) regime in a scenario considering multiple transmission and reception points (TRPs).

Chapter 4 concludes the dissertation, summarizing the main results and discussing potential future research lines.

The contributions of this work are listed as follows:

1. The application of a DNN-based beamforming (BF) strategy to solve the sum rate maximization problem assuming different levels of channel state information (CSI) imperfection in a MU-MISO system.

2. A robustness analysis of the adopted DNN, showing that it has a similar behavior under ICSI with respect to sum rate degradation when compared to the classical solutions. Also, a computational complexity comparison is provided.

3. The proposition of TRP-side DTX feature to assist terahertz (THz) systems facing overheating issues and network performance evaluation.

4. The investigation whether a particular system operating in a THz band can in fact deliver the expected increase in data rate, in comparison with a mmWave system with equal network layout.

1.2 Scientific contributions

The contents of this work, more specifically Chapter 2, have been partially published and presented with the following bibliographic information:

- SANTANA JR., E. de et al. On the robustness of deep learning based beamforming for MU-MISO systems. *In*: SIMPÓSIO BRASILEIRO DE TELECOMUNICAÇÕES E PROCESSAMENTO DE SINAIS (SBrT2021), XXXIX., 2021, Fortaleza. **Anais** [. . .]. Rio de Janeiro: Sociedade Brasileira de Telecomunicações, 2021. p. 1–5. DOI: 10.14209/sbrt.2021.1570730492

It is worth mentioning that this work was developed under the context of Ericsson/UFC technical cooperation project UFC.49 - WP3 Initial access and beam management above current NR bands, for which three technical reports have been delivered.

2 ROBUSTNESS ANALYSIS OF DEEP LEARNING BASED BEAMFORMING

This chapter addresses the problem of robust beamforming in MU-MISO systems. To this end, the performance of a DNN-based beamforming strategy under ICSI conditions in a MU-MISO scenario is assessed. A robustness analysis is provided by adding a controlled additive independent error term in the fast fading component of the channel, not changing its statistics. The DNN-based beamforming strategy is compared with the classical weighted minimum mean square error (WMMSE) solution in terms of the impact of ICSI on the average sum rate and computation complexity.

2.1 Introduction

For the evolution of wireless communication technologies, it is of greatest importance to optimize the resources and mechanisms of the network in order to provide robustness and better quality of service, and thus satisfy requirements of modern communication systems. 5G systems seek to provide reliable connectivity at any time in the most diverse scenarios [2], offering low latency, high transmission rates, and high mobility, even in denser networks where a high demand for data per user is present, outperforming previous generations and increasing the number of potential applications of mobile systems. The use of robust optimization techniques is essential to provide the proper and efficient functioning of these systems, ensuring that such requirements will be met.

BF is a means of exploiting antenna arrays to provide the expected performance gains, such as spatial multiplexing to one or multiple users in multi-antenna systems in 5G, e.g., by using optimization techniques [4]. One of these techniques focuses on the solution for the sum rate maximization problem subject to a total power constraint, which generally results in a non-convex numerical optimization problem.

Suboptimal solutions for that type of problem can be obtained via iterative algorithms such as WMMSE [5], given the optimal solution is usually hard to obtain and impractical for URLLC systems. However, iterative solutions have some drawbacks related to their computational complexity and delay, especially with the expected increase in the number of antennas in 5G systems. Thus, such classical beamforming techniques may be unable to meet the requirements of real time applications.

Such limitations motivate the search for alternative methods to ensure proper system operation. In this context, machine learning tools have been extensively employed to optimize modern wireless communication systems [6]. For instance, the employment of DNNs [7] is suitable to obtain the optimal beamforming in real time due to the possibility of an offline training model. In [8], a framework is proposed for optimal BF considering downlink (DL) transmission, where numerical results show gains with respect to computational complexity with satisfactory

performance in a set of common BF problems. However, the work in [8] does not provide any robustness analysis of the proposed DNN under ICSI conditions, which can severely limit the performance gain of BF techniques [9]. In [10], another type of machine learning strategy is applied to solve the rate maximization problem in a MU-MISO scenario. The authors show that deep Q-learning algorithms can learn a policy that can provide a robust BF structure, improving the performance of models based on perfect CSI in scenarios with ICSI. However, to achieve that goal, the deep Q-learning network needs to be trained from scratch for each execution after being deployed, while in [8] the DNN is designed to be applied directly after an offline training process.

This chapter assesses the application of a DNN-based beamforming strategy to solve the sum rate maximization problem assuming different levels of CSI imperfection in a MU-MISO system. A robustness analysis of the adopted DNN is provided, showing that it has a similar behavior under ICSI with respect to sum rate degradation when compared to the classical WMMSE solution. Also a comparison of the computational complexity in terms of execution time is presented.

The topics discussed in this chapter are organized as follows. Section 2.2 presents the system model and formulates the optimization problem. Section 2.3 is devoted to the beamforming strategies and describes the employed deep learning framework. In Section 2.4, the performance analysis and numerical results are presented an discussed. Finally, in Section 2.5, a summary is presented.

2.2 System model

A DL MU-MISO system has been considered, where a base station (BS) equipped with an antenna array with M omnidirectional antenna elements serves K user equipments (UEs), each with a single omnidirectional antenna as depicted in Fig. 1.

Figure 1 – A MU-MISO system where a single BS serves single antenna UEs within the coverage region.

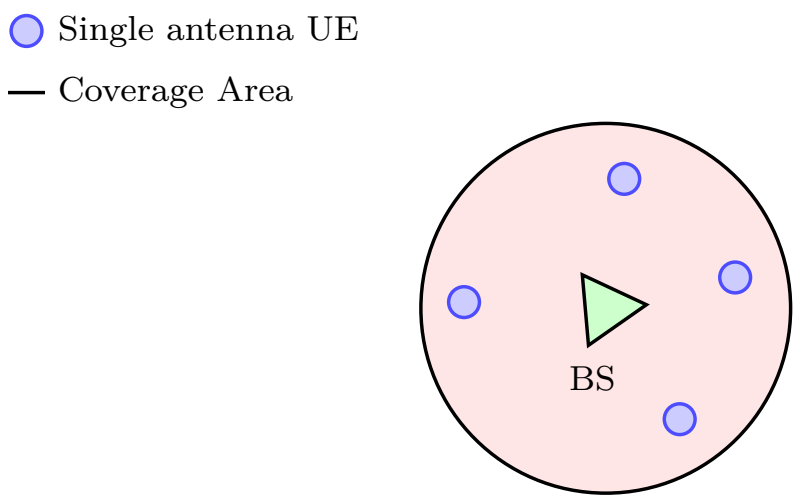

Source: Created by the author.

The channel between the BS and the k-th UE is given by

$$\mathbf{h}_k = \sqrt{g_k}\tilde{\mathbf{h}}_k\,, \tag{2.1}$$

where $\tilde{\mathbf{h}}_k \in \mathbb{C}^{M\times 1}$ denotes the fast fading component modeled by a complex Gaussian random vector with zero mean and covariance matrix $\mathbf{I}_M$, with $\mathbf{I}_M$ denoting an identity matrix of dimension $M \times M$, and g_k represents the large-scale fading gain.

The channel responses of the UEs are assumed to be known at the BS for beamforming purposes. An ICSI model is adopted by adding noise to the channel fading following the relation [11] [12]:

$$\hat{\mathbf{h}}_k = \sqrt{g_k}\left(\sqrt{1-\theta^2}\tilde{\mathbf{h}}_k + \theta\mathbf{h}_e\right), \tag{2.2}$$

where $\hat{\mathbf{h}}_k$ is the imperfect channel response of the k-th UE available at the BS, due to imperfect channel estimation of the direct link, $\mathbf{h}_e$ is the independent fast fading error component also modeled by a complex Gaussian random vector with zero mean and covariance matrix $\mathbf{I}_M$ uncorrelated with $\tilde{\mathbf{h}}_k$, and $0 \leq \theta \leq 1$ represents the accuracy of the channel estimation process. When $\theta = 0$ the channel estimate is perfect, whereas when θ is close to 1, more uncorrelated is the estimate with the actual channel. The linear combination in (2.2) ensures that $\mathbf{h}_k$ and $\hat{\mathbf{h}}_k$ have the same statistics.

For unicast data transmission, the BS applies the beamforming vector $\mathbf{w}_k \in \mathbb{C}^{M\times 1}$ to transmit the $M = K$ [1] independent data stream x_k to the k-th UE. Each data stream is considered to have $\mathbb{E}\{|x_k|^2\} = 1$, where $\mathbb{E}\{\cdot\}$ denotes the expected value operator.

The received signal at the k-th UE is given as follows:

$$y_k = \mathbf{h}_k^H \sum_{i=1}^{K} \mathbf{w}_i x_i + z_k, \tag{2.3}$$

where $(\cdot)^H$ denotes de conjugate transpose operation, z_k denotes the additive white Gaussian noise with zero mean and variance σ^2. The signal-to-interference-plus-noise ratio (SINR) at receiver k is defined as follows:

$$\gamma_k = \frac{|\mathbf{h}_k^H \mathbf{w}_k|^2}{\sum_{i=1, i\neq k}^{K} |\mathbf{h}_k^H \mathbf{w}_i|^2 + \sigma^2}. \tag{2.4}$$

2.2.1 Optimization problem and solution structure

In this scenario, the beamforming vectors are designed according to the following optimization problem [8]:

$$\begin{aligned} &\max_{\mathbf{w}_1,\ldots,\mathbf{w}_k} \sum_{k=1}^{K} \alpha_k \log_2\left(1+\gamma_k\right) \\ &\text{subject to } ||\mathbf{w}_k||^2 \leq P_{\max},\ \forall k \in \{1,\ldots,K\}. \end{aligned} \tag{2.5}$$

[1] Here, $M = K$ was set to provide for the system the maximum spatial degrees of freedom available.

The objective in (2.5) is to jointly find the beamforming vectors $\mathbf{w}_k$ that maximize the weighted sum rate $\sum_{k=1}^{K} \alpha_k \log_2\left(1+\gamma_k\right)$ subject to a transmit power constraint $P_{\max}$, where α_k represents constant system weights for the k-th UE.

For the problem (2.5), as well as in [8], the optimal beamforming vectors can be obtained through the solution structure presented in [13]:

$$\mathbf{w}_k^{\star} = \sqrt{p_k}\tilde{\mathbf{w}}_k = \sqrt{p_k}\frac{\mathbf{h}_k\left(\mathbf{I}_M + \sum_{j=1}^{K}\frac{\lambda_j}{\sigma^2}\mathbf{h}_j^H\mathbf{h}_j\right)^{-1}}{||\mathbf{h}_k\left(\mathbf{I}_M + \sum_{j=1}^{K}\frac{\lambda_j}{\sigma^2}\mathbf{h}_j^H\mathbf{h}_j\right)^{-1}||}. \tag{2.6}$$

To formulate this particular closed form expression, first the following power minimization problem for the presented scenario is considered:

$$\begin{aligned} &\min_{\mathbf{w}_1,\ldots,\gamma_k} \sum_{k=1}^{K} ||\gamma_k||^2 \\ &\text{subject to } \gamma_k \geq \gamma_k', \forall k \in \{1,\ldots,K\}. \end{aligned} \tag{2.7}$$

Here, the constraints $\gamma_1', \ldots, \gamma_k'$ represent the target SINR that each user shall achieve at the optimum. Reformulating (2.7) as a convex problem, by extracting the convexity of the SINR constraints and considering the inner product $\mathbf{h}_k^H\gamma_k$ real valued and positive, it is possible to rewrite $\gamma_k \geq \gamma_k'$ using (2.4) as

$$\frac{\mathbf{h}_k^H\gamma_k}{\sqrt{\gamma_k'\sigma^2}} \geq \sqrt{\sum_{i=1,i\neq k}^{K}\frac{1}{\sigma^2}|\mathbf{h}_k^H\mathbf{w}_i|^2 + 1}\,. \tag{2.8}$$

By defining the Lagrangian function of the reformulated convex problem as

$$\mathcal{L}\left(\mathbf{w}_1,\ldots,\gamma_k,\lambda_1,\ldots,\lambda_K\right) = \sum_{k=1}^{K}||\gamma_k||^2 + \sum_{k=1}^{K}\lambda_k\left(\sum_{i=1,i\neq k}^{K}\frac{1}{\sigma^2}|\mathbf{h}_k^H\mathbf{w}_i|^2 + 1 - \frac{\mathbf{h}_k^H\gamma_k}{\sqrt{\gamma_k'\sigma^2}}\right), \tag{2.9}$$

it can be seen that the dual function is $\min_{\mathbf{w}_1,\ldots,\gamma_k}\mathcal{L} = \sum_{k=1}^{K}\lambda_k$ and the strong duality relation [13] implies that $\sum_{k=1}^{K}p_k = \sum_{k=1}^{K}\lambda_k = P_{\max}$ at the optimal solution.

By applying the Karush–Kuhn–Tucker (KKT) conditions to solve (2.7), $\partial\mathcal{L}/\partial\gamma_k = 0$, for $k = 1,\ldots,K$, it is possible to obtain the solution structure in (2.6), since the solution to problem (2.7) will also solve (2.5) [14].

According to the solution structure in (2.6), the optimal beamforming vector for the k-th UE is composed of a set of key parameters: a power factor p_k, a unitary vector that indicates the beamforming direction $\tilde{\mathbf{w}}_k$, and the variable λ_j, which represents the Lagrange multipliers for the rate maximization dual problem, as indicated by the strong duality relation discussed above.

2.3 Multi-user beamforming strategies

As seen in the previous section, it is necessary to find the precoding vectors that maximize the sum rate of all users to solve the optimization problem (2.5). This type of problem

is well known in the literature [5], [15], and the process for obtaining an optimal solution is quite complex due to the non-convex nature of the optimization problem. The beamforming strategies considered in this chapter are presented in the following.

2.3.1 WMMSE beamforming

Suboptimal solutions to problem (2.5) can be found via iterative methods such as the WMMSE algorithm described in [5]. To solve the weighted sum rate (WSR) maximization problem for each user rate in the MU-MISO scenario, the WMMSE algorithm will be considered.

As described in [5], the algorithm alternately iterates between the WMMSE transmit filter, the receive filter that minimizes the mean square error (MSE) of the transmit data, and the update of the weight matrix through closed form expressions, exploiting the relationship between the WMMSE and WSR optimization problems to obtain the beamforming vectors.

In the considered scenario, the beamforming matrix $\mathbf{W} = [\mathbf{w}_1, ..., \mathbf{w}_k]$ is given by [5]:

$$\mathbf{W} = \left(\mathbf{H}^H\mathbf{V}^H\mathbf{U}\mathbf{V}\mathbf{H} + \frac{\mathrm{Tr}(\mathbf{U}\mathbf{V}\mathbf{V}^H)}{P_{\max}}\mathbf{I}_M\right)^{-1}\mathbf{H}^H\mathbf{V}^H\mathbf{U}, \tag{2.10}$$

where $\mathbf{U} = \mathrm{diag}\{u_1, ..., u_k\}$ and $\mathbf{V} = \mathrm{diag}\{v_1, ..., v_k\}$ are the diagonal matrices containing the user WMMSE weights and the MSE filter coefficients, respectively, and $\mathrm{Tr}(\cdot)$ stands for the trace of the argument matrix. The combination of these weights and filter coefficients will be used as output values in order to train the neural network.

2.3.2 Deep learning based beamforming framework

In [8], a multi-user beamforming solution is proposed, which considers the MU-MISO case and employs a machine learning strategy, more precisely, a deep neural network. This strategy allows the learning of suboptimal beamforming vectors in real time with a good performance and less computational delay, assuming that offline training models will be used in real time applications.

Based on the sum rate maximization strategy proposed in [8], this chapter assumes a supervised model that has as input the channel samples between the BS and each UE, and as output values the key parameters λ_k and p_k of the beamforming vectors from (2.6). Hence, it is possible to recover the beamforming vector using the DNN output and the channel samples.

The output values λ_k and p_k are extracted from the solution given by the WMMSE algorithm presented in (2.10) to be used in the training of the supervised model. The transmit power values p_k can be extracted directly from the columns of the beamforming matrix $\mathbf{W}$ as follows

$$p_k = ||\mathbf{w}_k||^2, \tag{2.11}$$

whereas the variables λ_k can be interpreted as user priorities [13] and are given by

$$\lambda_k = P_{\max}\left|\frac{u_k v_k v_k^*}{Tr(\mathbf{U}\mathbf{V}\mathbf{V}^H)}\right|, \tag{2.12}$$

Figure 2 – DNN framework for downlink beamforming.

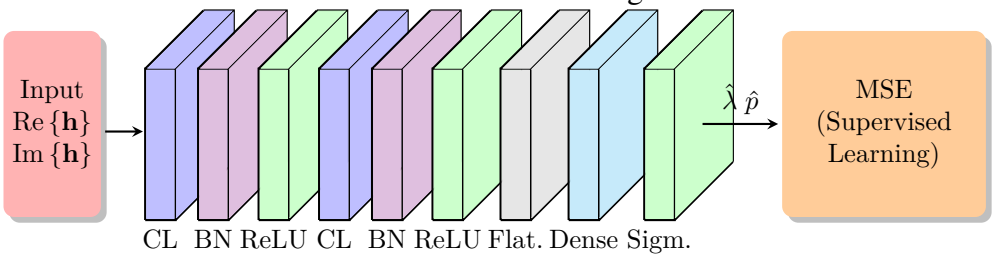

Source: Created by the author.

where $(\cdot)^*$ stands for the complex conjugate operator.

For the construction of the neural network models we consider a DNN structure as illustrated in Fig. 2 which uses supervised learning to estimate the output values (λ_k, p_k) considering the MSE metric.

Based on [8], the layers that make up the proposed model are listed below.

- **Input layer:** The complex channel coefficients between the BS and all UEs are stacked into a channel data vector, e.g. $\mathbf{h} = \left[\mathbf{h}_1^T, ..., \mathbf{h}_K^T\right]^T \in \mathbb{C}^{MK\times 1}$, and then separated into real and imaginary components before they are fed in batches into the neural network. Then, the input data of the neural network are in the form $\left[\mathrm{Re}\{\mathbf{h}\}, \mathrm{Im}\{\mathbf{h}\}\right]^T \in \mathbb{R}^{2\times MK}$.

- **Convolutional Layers:** In each convolutional layer the input layer is convolved with the convolutional kernels, and their parameters, such as weights and bias, are shared among different channel coefficients to extract the features.

- **Batch Normalization layers:** The normalization layers are introduced after each convolutional layer to normalize their output by subtracting the batch mean and dividing by the batch standard deviation. As described in [8], these layers help to reduce the probability of over-fitting, to enable a higher learning rate, and to make the neural network less sensitive to the initialization of weights.

- **Activation (Ac.) layers:** These layers are introduced after the batch normalization layers to apply the rectified linear unit (ReLU) or sigmoid function to the input.

- **Flatten Layer and Fully-connected Layer:** The former is used to reshape its input to a vector that will be interpreted by the fully-connected layer, that applies the weights and the biases from its neurons to its input.

- **Output layer:** Here the predicted key parameters vector $\left[\hat{\mathbf{p}}^T, \hat{\boldsymbol{\lambda}}^T\right]^T \in \mathbb{R}^{2K\times 1}$ are generated, where $\hat{\mathbf{p}}$ and $\hat{\boldsymbol{\lambda}}$ are the vectors containing the power and the weights of all users respectively, and the MSE loss function is applied finishing the learning process.

After applying the trained model to the channel samples, the predicted output values are converted to suboptimal key parameters by a scaling process to meet the power constraint using the following expressions:

$$\hat{\mathbf{p}}^{\star} = \frac{P_{\max}}{||\hat{\mathbf{p}}||_1}\hat{\mathbf{p}} \text{ and } \hat{\boldsymbol{\lambda}}^{\star} = \frac{P_{\max}}{||\hat{\boldsymbol{\lambda}}||_1}\hat{\boldsymbol{\lambda}}, \tag{2.13}$$

where $||\cdot||_1$ stands for the ℓ_1 norm operator.

With the scaled parameters, the optimum solution structure (2.6) is applied to recover the estimated optimum beamforming vector $\mathbf{w}_k^{\star}$ considering the values of $\hat{\boldsymbol{\lambda}}^{\star}$ and $\hat{\mathbf{p}}^{\star}$ defined in (2.13).

Table 1 – Neural Network layer parameters.

# Layer	Description
1. Input Layer	Size = $2 \times MK$; 200 batches; 100 epochs
2. Convolutional Layer (CL)	8 (3×3) kernels with padding (1, 1); stride 1
3. Batch Normalization Layer (BN)	Momentum = 0.99; $\varepsilon = 0.001$
4. Activation Layer	ReLU
5. Convolutional Layer (CL)	8 (3×3) kernels with zero padding 1; stride 1
6. Batch Normalization Layer (BN)	Momentun = 0.99; $\varepsilon = 0.001$
7. Activation Layer	ReLU
8. Flatten Layer	
9. Fully-connected Layer	Dense with $2K$ neurons
10. Activation Layer	Sigmoid
11. Output Layer	MSE metric; Adam optimizer with learning rate of 0.001

Source: Created by the author.

2.4 Simulation results

In order to assess the performance of the BF strategies and evaluate their robustness considering ICSI, we consider the DL transmission system described in Section 2.2 composed of a single BS equipped with $M = 4$ antennas that serves $K = 4$ single antenna UEs. The large scale fading component g_k follows the model $g_k = 128.1 + 37.6\log_{10}(r_k)$[dB] [16] where r_k is the distance in km between the BS and the k-th UE. UE positions are generated uniformly inside a circle of radius 500 m and centered at the BS position, considering a minimum distance of 100 m from the BS, the considered noise power spectral density is -174 dBm/Hz, and the system bandwidth is 20 MHz. The simulation parameters are summarized in Table 2.

For the training of the DNN models, a set of $25,000$ samples ($\mathbf{h}$, $[\lambda, p]$) were considered, with a train-test split ratio of 80%/20%. As in [8], the weights of the network layers were initialized following a Glorot normal distribution and the biases initially set to 0. Also, data normalization is applied by scaling the channel samples by the noise power. The targets were divided by a factor to ensure that they are contained within the interval $[0, 1)$ to guarantee numerical stability. The other parameters of the neural network are described in Table 1. The DNN models and the benchmarks were implemented using Python 3.8 with Tensorflow

Table 2 – Simulation Parameters.

Number of BS antennas M	4
Number of single antenna UEs K	4
Cell radius	500 m
UE-BS minimum distance	100 m cf. [8]
System bandwidth	20 MHz
Noise power spectral density	−174 dBm/Hz

Source: Created by the author.

2.4, Keras 2.4.3 and Numpy 1.20 as numerical computing library on a computer with 1 AMD Ryzen5-3600X CPU and RAM of 32 GB.

To compare the performance of the BF strategies as solution for the optimization problem (2.5), the zero-forcing (ZF) and regularized zero-forcing (RZF) [13] solutions with equal power allocation were considered as well as the WMMSE beamforming with the initialization based on RZF and the system weights $\alpha_k = 1$ as baseline solutions for comparing with the DNN beamforming strategy. Also, the target key parameters were extracted from the WMMSE solution to compose the training and test sets.

All the results were generated considering the average of $5,000$ experiments. In Fig. 3 it is observed that with the increase in the transmitted power there is an increase in the sum rate performance, with the DNN solution showing itself as an upper limit for the RZF solution and close to the WMMSE target for low signal-to-noise ratio (SNR). In this case, the supervised learning solution tries to approach the WMMSE solution as much as possible, but its performance is upper limited by the WMMSE and lower bounded by the WMMSE initialization, showing the potential of the DNN beamforming.

In Fig. 4, the execution time of the BF strategies is presented. As the number of transmit antennas increases, the DNN BF applied after an offline training process has a reduced computational complexity in comparison with the iterative WMMSE solution. The ZF and RZF presented the best execution times due to their vectorized implementation. The main source of complexity in the DNN BF computations is the recovery process using (2.6).

For the robustnesss analysis of the supervised learning solution, the ICSI model (2.2) was considered, with the WMMSE performance as a benchmark. First, we perform the experiments applying the WMMSE solution obtained using $\hat{\mathbf{h}}_k$, varying the parameter θ between $[0, 1]$, and compute the error between the average achieved sum rate and the sum rate that would be achieved when considering perfect CSI.

To investigate the performance of the DNN beamforming, we consider $\hat{\mathbf{h}}_k$ as the input model for the precoder prediction. Then, we compute the average sum rate and the error considering the predicted precoder using perfect CSI samples.

The relative error (%) results for both the WMMSE and DNN beamforming are summarized in tables 3 and 4. It can be seen that the relative error obtained using the DNN solution increases as much as the error obtained using WMMSE with the evolution of the transmit power. This behavior indicates that the channel estimation error, which follows the same

Figure 3 – Sum rate performance comparison considering a system with $M = K = 4$.

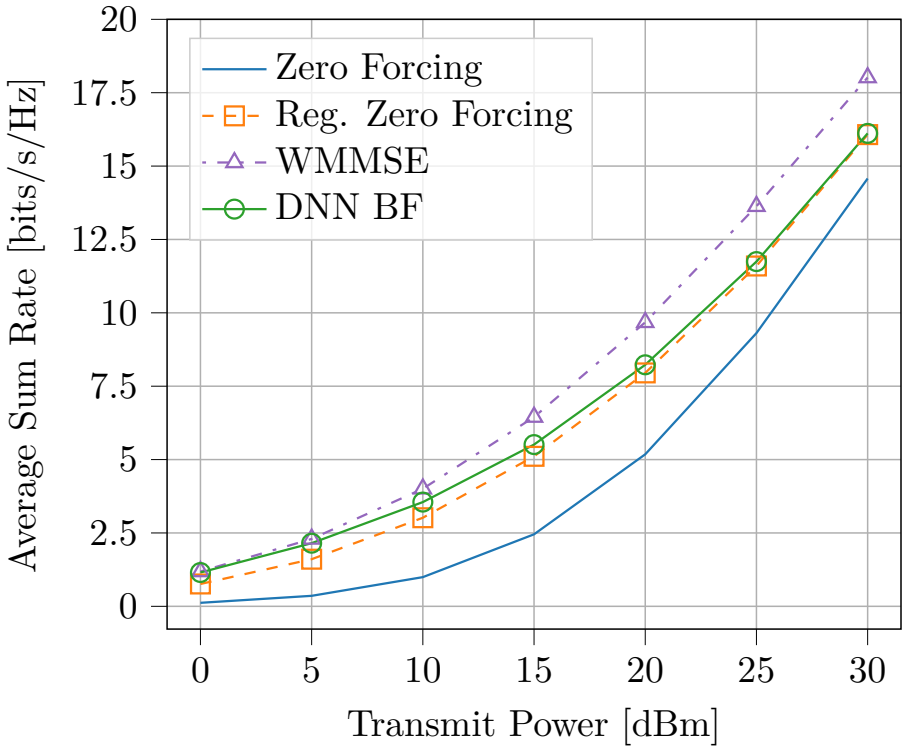

Source: Created by the author.

Figure 4 – Execution time per sample considering a system with $P_{\max} = 30$ dBm and $M = K$.

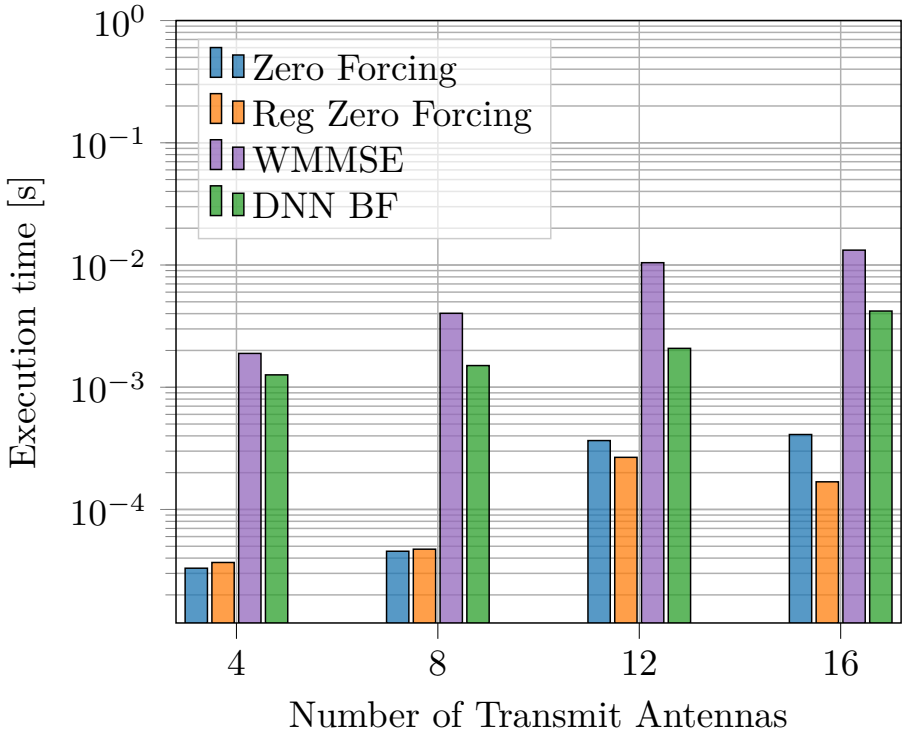

Source: Created by the author.

statistical distribution of the channel coefficients, has a similar effect on both solutions.

Table 3 – Average Sum Rate Error due to ICSI for each $P_{\max}$ - WMMSE BF.

	0 dBm	5 dBm	10 dBm	15 dBm	20 dBm	25 dBm	30 dBm
$\theta = 0$	0.00	0.00	0.00	0.00	0.00	0.00	0.00
$\theta = 0.25$	3.85	4.12	5.86	9.66	15.83	25.31	37.51
$\theta = 0.5$	15.19	16.05	20.65	29.14	40.13	52.38	63.99
$\theta = 0.75$	33.56	35.48	41.59	51.42	61.89	71.53	79.16
$\theta = 1$	61.86	62.89	67.96	75.17	81.31	85.91	89.28

Source: Created by the author.

Table 4 – Average Sum Rate Error due to ICSI for each $P_{\max}$ - DNN BF

	0 dBm	5 dBm	10 dBm	15 dBm	20 dBm	25 dBm	30 dBm
$\theta = 0$	0.00	0.00	0.00	0.00	0.00	0.00	0.00
$\theta = 0.25$	3.58	3.51	4.97	7.98	13.46	23.45	37.55
$\theta = 0.5$	14.40	14.33	18.59	26.31	37.09	51.01	64.42
$\theta = 0.75$	32.82	32.43	39.04	49.03	59.66	70.58	79.30
$\theta = 1$	60.82	60.45	66.83	74.20	79.84	84.70	88.58

Source: Created by the author.

Figure 5 – Sum rate performance for WMMSE (dashed patterns) and DNN BFs (solid) in presence of different levels of ICSI controlled by the variable θ.

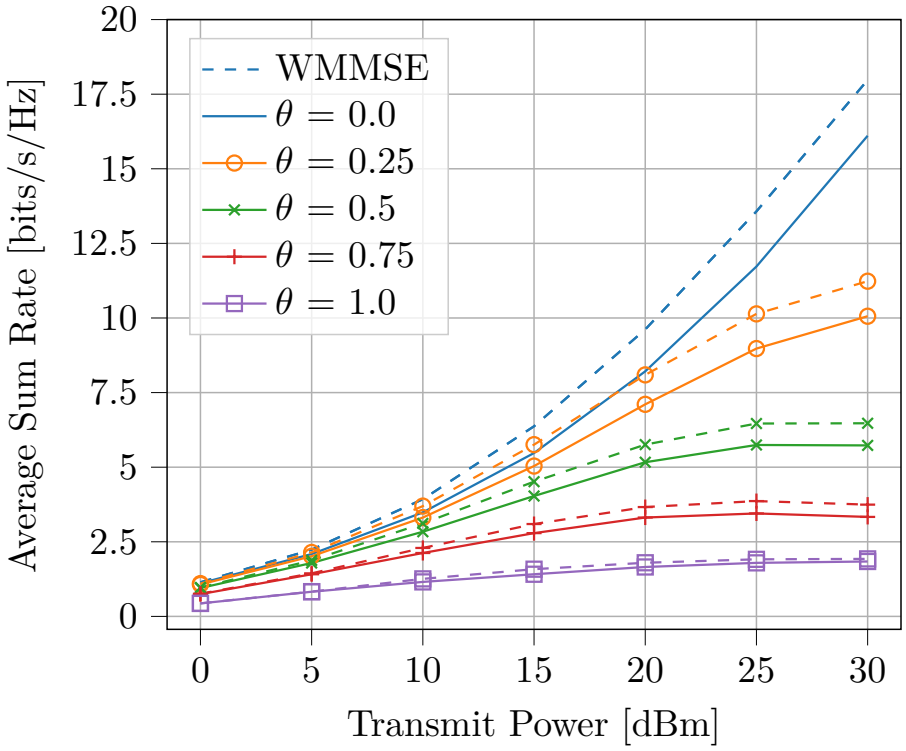

Source: Created by the author.

For each value of θ, the sum rate performance of the beamforming solutions is presented in Fig. 5. The DNN based precoder performance is close to that of WMMSE for low SNRs as in Fig. 3, and the sum rate curve behavior in the presence of channel estimation error shows that with the increase of θ, both strategies are similarly penalized, with the WMMSE performing better than the supervised solution as expected.

2.5 Chapter summary

In this chapter, the performance of a DNN BF solution was assessed for a MU-MISO system under ICSI. The ICSI was modeled as a combination of the actual channel with a controlled noisy term. The focus was on the maximization of the weighted sum rate, which is by definition a non-convex problem whose parameterized optimal solution is hard to be obtained. The DNN BF applied to obtain a suboptimal solution is drawn from a DNN whose input is the channel response and output is the beamforming vector parameters, while the (noisy) channel is assumed to be known at the BS. The results indicate that the deep learning based beamforming solution is viable and as robust as the WMMSE, assuming that the channel and ICSI models follow the same distribution.

3 NETWORK PERFORMANCE EVALUATION UNDER DYNAMIC DTX

This chapter evaluates the network performance of a cellular system operating at 100 GHz with bandwidth of around 3 GHz under a dynamic TRP-side DTX regime. The use of THz bands are envisioned as a means to achieve higher data rates in 6G systems. To deal with more severe propagation conditions in THz bands, a network with multiple TRPs equipped with large antenna arrays serving multi-panel UEs is adopted. However, in this network setup, the power consumption at TRPs' radio components packed with several antenna elements significantly increases due to the very high processing burden in such a wide bandwidth. To avoid overheating issues, a TRP-side DTX method is proposed, which controls the amount of downlink slot transmissions while guaranteeing cell-specific reference signal transmissions. Simulation results considering different DTX settings and traffic loads will be presented and discussed.

3.1 Introduction

For the evolution of wireless communication systems beyond 5G, THz bands are envisioned as a potential technology in order to meet the requirements of future systems, such as extremely high data rates [17].

The wide range of frequencies available in THz bands in comparison with the NR frequency range 2 (FR2) bands is the main aspect considered to reach data rates in the order of terabits-per-second. However, exploring high-frequency bands becomes challenging due to severe propagation conditions, subject to increased signal attenuation due to scatterers and obstacles within the radio link [18]. To properly operate in high frequency, the system needs to provide enough beamforming gain through high directive beams by employing very-large antenna arrays [19], specially at TRPs. On the UE side, they are typically equipped with multiple antenna panels to obtain a good spherical coverage.

With beam-based transmissions in high-frequency bands, beam management (BM) [1] is leveraged in the initial 3rd generation partnership project (3GPP) release of NR 5G. The BM task is to establish and maintain narrow beam pair links (BPLs) with suitable channel conditions through its procedures [20] in order to provide UEs proper network access. Moreover, TRPs are currently equipped with NR massive MIMO radios that consist of self contained units in which the antenna panel and its processing units are coupled in a single box all together [21]. An efficient cooling system is paramount for such a compact design, as several heat sources close to one another can lead to a fast increase in the device temperature.

However, the exploitation of wider system bandwidths in THz bands requires the use of more computational resources. Critical computations such as analog-to-digital (AD)/digital-to-analog (DA) conversions and power amplifier linearization (e.g., digital predistortion) using higher sampling rates make the radio processing unit operate in a higher clock regime, thus

consuming much more power [22, 23]. As a consequence, the amount of dissipated energy converted into heat might expose radio components of current NR massive MIMO radios to overheating conditions when operating in THz bands, which can limit the overall system performance.

In the literature, several works deal with thermal and/or energy issues by introducing transmission/reception discontinuities. Particularly, discontinuous reception (DRX) is commonly adopted at UEs to increase their power efficiency whenever there is no data to deliver to them, as in [24]. On the other hand, DTX is usually adopted at base stations to decrease the network energy consumption whenever there is no traffic/signaling to transmit to UEs, as discussed in [25], or based on a resource utilization as in [26].

Nevertheless, to the best of the author's knowledge, current DTX/DRX approaches do not cope with the significant increase in power consumption added by the system operation in THz bands from a network perspective. That is, TRPs equipped with NR massive MIMO radios are likely to suffer from overheating by simply serving UEs in THz bands with wide system bandwidths in the order of gigahertz. Consequently, the problem here is a matter of preventing TRPs from overheating whenever they need to stay active during several time slots.

Therefore, the contributions of this chapter are twofold. First, the use of TRP-side DTX is proposed for a TRP radio unit to i) be inactive whenever there is no traffic to transmit from it; ii) turn off if a pre-determined number of accumulated time slots is transmitted by it. Hence, the TRP radio unit can cool down, avoiding overheating issues. Second, this chapter investigates whether a particular system operating in a THz band can in fact deliver the expected increase in data rate, in comparison with a mmWave system with equal network layout, under the thermal limitations controlled by TRP DTX. To this end, different system-level metrics are evaluated, such as UE throughput, mean block error rate (BLER) and SINR.

The rest of the chapter is organized as follows. In Section 3.2 the system model is described. The proposed TRP DTX framework is presented in Section 3.3. In Section 3.4 the applied BM procedures and the considered system level aspects are introduced. The system level evaluation and the numerical results are presented in Section 3.5. Finally, in Section 3.6 a summary is presented.

3.2 System model

Consider a beam-based, orthogonal frequency division multiplexing (OFDM) cellular system [1] where TRPs in a TRP set $\mathcal{M}$, forming a coordination cluster, serve UEs in a downlink THz band. The system operates at $f_c = 100$ GHz with a resource block (RB) set $\mathcal{Q}$ with $N_{\mathrm{RB}} = 264$ RBs [1] available for traffic with subcarrier spacing $L_{\mathrm{sc}} = 960$ kHz, yielding a wide system bandwidth $L_{\mathrm{BW}} \approx 3$ GHz, and $N_{\mathrm{slot}} = 64$ slots within a subframe of 1ms.

[1] An RB corresponds to 12 subcarriers, while a slot, the basis of a transmit time interval (TTI), denotes 14 OFDM symbols, resulting in a 12×14 grid of resource elements herein referred to as a physical resource block (PRB).

Figure 6 – Multi-TRP network with 3 TRPs forming a coordination cluster comprising a single BBU/scheduler with UEs in a hotspot region delimited by the red dashed curve.

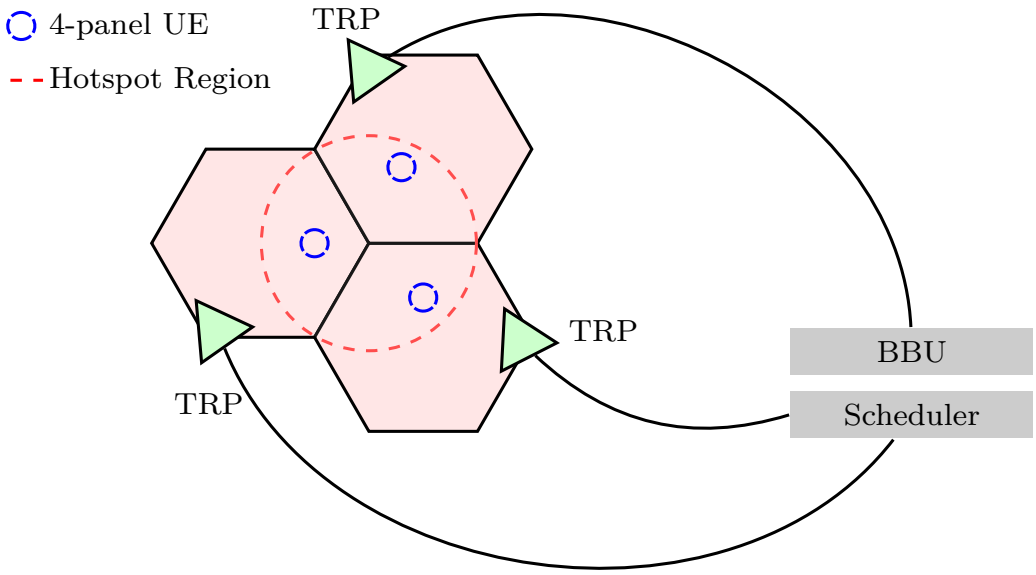

Source: Created by the author.

The coordination cluster has a hexagon layout with three TRPs, i.e., $|\mathcal{M}| = 3$, positioned to cover a hexagonal sector, as illustrated in Fig. 6. They are connected with a base station that has single baseband unit (BBU) where a time division multiplex (TDM)-based UE scheduler is implemented in a centralized manner with ideal backhaul.

Both TRPs and UEs are equipped with panels of dual-polarized uniform rectangular array (URA) panels whose cross-pole elements have identical radiation patterns and are coupled to one radio frequency (RF) chain per polarization, which means two digital ports in total per transmitter/receiver. Specifically, each TRP is equipped with a single URA panel with N_t cross-pole elements, while UEs are equipped with four URA panels with N_r cross-pole elements, increasing the probability to find good signal reception for different TRPs. For simplicity, the panel of a single-panel TRP will in this text be referred to simply as a TRP.

In order to increase the chance that UEs experience good coverage from any of the TRPs, UE positioning follows a uniform distribution inside the "hotspot" depicted in Fig. 6 by the red dashed curve. Besides, a UE has its panels oriented perpendicularly to the Cartesian xy-plane, each pointing to a different UE side (left, right, front and back), with arbitrary rotation angle with respect to the z-axis.

To provide cell coverage, TRPs periodically transmit cell-specific synchronization signals (SSs) for UEs to establish a BPL. A number of L^{SS} time-multiplexed SSs are transmitted in bursts of $L^{\mathrm{SS}}/4$ slots every T^{SS} ms via beam sweeping from all TRPs in a synchronized fashion. Between two consecutive SS bursts, TRPs also transmit UE-specific reference signals (RSs),

also via beam sweeping, to cope with BPL quality degradation due to, e.g., blockage and UE rotation/movements.

3.2.1 Channel model

As for the channel model, the link between the digital ports of a pair of TRP and UE panels denotes – after signal combining – a single MIMO layer that performs wideband hybrid beamforming (HBF). Let $h_{m,k,b}[q,j,l] \in \mathbb{C}$ be the equivalent channel response between the linearly combined digital ports of TRP m and the b-th panel of UE k at RB q and l-th OFDM symbol of slot j, defined as:

$$h_{m,k,b}[q,j,l] = \left(\mathbf{w}_{k,b}[j,l]\right)^H \mathbf{H}_{m,k,b}[q,j]\mathbf{f}_m[j,l]\,, \tag{3.1}$$

where $\mathbf{w}_{k,b}[j,l] \in \mathbb{C}^{2N_r \times 1}$ and $\mathbf{f}_m[j,l] \in \mathbb{C}^{2N_t \times 1}$ are the dual-polarization beams of the b-th panel of UE k and TRP m, respectively, while $\mathbf{H}_{m,k,b}[q,j] \in \mathbb{C}^{2N_r \times 2N_t}$ denotes the dual-polarization channel matrix in the frequency domain, which is defined as:

$$\mathbf{H}_{m,k,b}[q,j] = \begin{bmatrix} \tilde{\mathbf{H}}^{(1,1)}_{m,k,b}[q,j] & \tilde{\mathbf{H}}^{(1,2)}_{m,k,b}[q,j] \\ \tilde{\mathbf{H}}^{(2,1)}_{m,k,b}[q,j] & \tilde{\mathbf{H}}^{(2,2)}_{m,k,b}[q,j] \end{bmatrix}, \tag{3.2}$$

where $\tilde{\mathbf{H}}^{(\alpha,\beta)}_{m,k,b}[q,j] \in \mathbb{C}^{N_r \times N_t}$, with $(\alpha,\beta) \in \{1,2\} \times \{1,2\}$ representing the per polarization pair, are the matrices storing the channel coefficients between the antenna elements of the m-th TRP and the b-th panel of the k-th UE.

These coefficients are composed of both large and small scale components, following the channel model described in [27] with space-time consistency according to the 3GPP consistency procedure B [28] and spatially-consistent random variables generated as in [29, 30]. It also includes the stochastic blockage model A as in [28] and UE panel blockage [2] as in [31].

Note that all beams in (3.1) are wideband, i.e., not indexed by q, unit-norm, constant-modulus vectors and selected on an OFDM symbol basis, i.e., indexed by j and l. At last, $\mathbf{H}_{m,k,b}[q,j]$ is assumed flat within the corresponding physical resource block (PRB), i.e., not indexed by l.

3.2.2 Signal model

For beam-based transmissions, a pair of beams $\mathbf{f}_m[j,l]$ and $\mathbf{w}_{k,b}[j,l]$ should be selected, then forming a BPL. Such beams can have either wide beamwidth/small beamforming gain or narrow beamwidth/large beamforming gain. For wide beams, the beam widening technique in [32] is adopted. Beam widening exploits the tradeoff between beamwidth and beamforming gain. On one hand, the same analog beam can be applied in both polarizations, then increasing the beamforming gain. On the other hand, dual polarized beamforming (DPBF) [32] applies a different analog beam per polarization, which widens beams at the cost of less beamforming gain.

[2] For each UE, one of its panels is randomly selected to have its large-scale channel component multiplied by a 0.1 attenuation factor.

3.2.2.1 Narrow beam codebook

Let $\mathcal{B}_{N_t,2} \subset \mathbb{C}^{2N_t}$ be the set of TRP narrow beams, defined as

$$\mathcal{B}_{N_t,2} = \left\{ \mathbf{b} \middle| \mathbf{b} = \begin{bmatrix} \mathbf{c}^T & \mathbf{c}^T \end{bmatrix}^T, \forall \mathbf{c} \in \mathcal{D}_{N_t,2} \right\}, \tag{3.3}$$

where $\mathcal{D}_{N_t,2}$ is the set of all column vectors of an $N_t \times 2N_t$ discrete Fourier transform (DFT) matrix with oversampling factor of 2. Thus, whenever a TRP narrow beam should be selected, $\mathbf{f}_m[j,l] \in \mathcal{B}_{N_t,2}$. Similarly, the set of UE narrow receive beams can be defined as $\mathcal{B}_{N_r,1} \subset \mathbb{C}^{2N_r}$,

$$\mathcal{B}_{N_r,1} = \left\{ \mathbf{b} \middle| \mathbf{b} = \begin{bmatrix} \mathbf{c}^T & \mathbf{c}^T \end{bmatrix}^T, \forall \mathbf{c} \in \mathcal{D}_{N_r,1} \right\}, \tag{3.4}$$

where $\mathcal{D}_{N_r,1}$ is the set of all column vectors of an $N_r \times N_r$ DFT matrix with factor set to 1. Thus, whenever a UE narrow beam should be selected, $\mathbf{w}_{k,b}[j,l] \in \mathcal{B}_{N_r,1}$.

3.2.2.2 Wide beam codebook

Let $\mathcal{A}_{N_t,2} \subset \mathbb{C}^{2N_t}$ be the set of TRP wide beams obtained as in [32] – assuming a protoarray with half of the antenna elements in each TRP URA dimension and column vectors of an $N_t/4 \times 2N_t$ DFT matrix with oversampling factor of 2. Thus, whenever a TRP wide beam should be selected, $\mathbf{f}_m[j,l] \in \mathcal{A}_{N_t,2}$. Similarly, the set of UE wide beams can be defined as $\mathcal{A}_{N_r,1} \subset \mathbb{C}^{N_r}$, assuming a protoarray with half of the antenna elements in each UE URA dimension and column vectors of an $N_r/4 \times N_r$ DFT matrix with oversampling factor of 1. Thus, whenever a UE wide beam should be selected, $\mathbf{w}_{k,b}[j,l] \in \mathcal{A}_{N_r,1}$.

3.2.2.3 Received signal model

Considering that the state of a TRP can be changed during the DTX regime, the received signal $y_{k,b,m}[q,j,l] \in \mathbb{C}$ at the combined digital ports switched to the b-th panel of UE k from TRP $m \in \tilde{\mathcal{M}}_j$ sampled at RB q and l-th OFDM symbol of slot j, is herein defined as:

$$y_{k,b,m}[q,j,l] = h_{m,k,b}[q,j,l]s_m[q,j,l] + \sum_{\substack{\bar{m} \in \tilde{\mathcal{M}}_j \\ \bar{m} \neq m}} h_{\bar{m},k,b}[q,j,l]s_{\bar{m}}[q,j,l] + n_k[q,j,l], \tag{3.5}$$

where $s_m[q,j,l] \in \mathbb{C}$, for every TRP m forming the set of available TRPs $\tilde{\mathcal{M}}_j$, denotes the single MIMO stream symbols from TRPs with power constraint $\mathbb{E}\left\{|s_m[q,j,l]|^2\right\} = \frac{P_{\text{TX}}}{N_{\text{RB}}}$, where P_{TX} is the available TRP transmit power, and $n_k[q,j,l]$ is an i.i.d. $\mathcal{CN}(0,\sigma_n^2)$ noise. Also $h_{m,k,b}[q,j,l]$ is assumed to be perfectly known.

3.2.2.4 RSRP measurement

When the symbol $s_m[q,j,l]$ is known by the UE, such as those conveyed by SSs, the signal quality can be measured from the received power. Let $\psi_{k,b,m}[j,l]$ be the reference

signal received power (RSRP) of the received signal at the b-th panel of UE k from TRP $m \in \tilde{\mathcal{M}}_j$ sampled at RBs $q \in \mathcal{Q}_{\text{RS}} \subset \mathcal{Q}$ and l-th OFDM symbol of slot j, defined as:

$$\psi_{k,b,m}[j,l] = \frac{1}{|\mathcal{Q}_{\text{RS}}|} \sum_{q \in \mathcal{Q}_{\text{RS}}} \left| h_{m,k,b}[q,j,l] \right|^2 . \tag{3.6}$$

RSRP measurements in (3.6) are used as a beam selection criterion to i) establish a BPL, and ii) keep/adjust that BPL by selecting better beams for subsequent transmissions.

3.2.2.5 SINR measurement

A beam pair for traffic is selected on a slot basis. That is, $\mathbf{f}_m[j,l]$ and $\mathbf{w}_{k,b}[j,l]$ are kept fixed in any OFDM symbol l' conveying data symbols within slot j. The corresponding SINR sampled at RB q, $\forall l' \in \mathcal{S}_j^{\text{data}}$, is then defined as

$$\gamma_{k,b,m}[q,j] = \frac{\left| h_{m,k,b}[q,j,l'] \right|^2}{\sum_{\substack{\bar{m} \in \tilde{\mathcal{M}}_j \\ \bar{m} \neq m}} \left| h_{\bar{m},k,b}[q,j,l'] \right|^2 + \sigma_n^2} , \tag{3.7}$$

where $\mathcal{S}_j^{\text{data}}$ stands for the subset of OFDM symbols of slot j that convey data.

3.2.3 Problem statement

This work assumes that a TRP operating in a THz band uses similar radio unit technology of current NR MIMO antennas. Then, a problem emerges: a TRP i) *consumes/dissipates* much more power due to sampling operations in wider[3] system bandwidth, and thus ii) *overheats*[4] whenever it consecutively transmits a number of slots larger than a pre-determined threshold $n^{\max}$.

TRP DTX is herein utilized as the *solution tool* to avoid overheating issues by switching off a TRP m, on a slot basis, whenever its threshold $n^{\max}$ is reached. Such a threshold is set large enough for TRPs to at least transmit all SSs – assuming that in such a case they do not overheat – but not too large, e.g., less than the number of slots within the T^{SS} window. Thus, TRPs that can be active to transmit at slot j, i.e., those not switched-off by DTX in a previous slot, form the subset $\tilde{\mathcal{M}}_j \in \mathcal{M}$.

It is worth noting that both RSRP and SINR in (3.6) and (3.7), respectively, depend on the resulting subset $\tilde{\mathcal{M}}_j$, which implies that TRP DTX has an important impact on the system performance. The proposed TRP DTX method will be discussed in detail in the following section.

---

[3] In mmWave bands, L_{sc} is up to 240 kHz, while herein L_{sc} = 960 kHz. For a constant Q, the bandwidth in the THz band is then wider.

[4] This work does not rely on any thermal model to quantitatively evaluate overheating issues and to determine $n^{\max}$ values.

3.3 Dynamic TRP DTX method

Methods to control the hardware temperature at radio units operating in THz bands are essential to preserve their functionality and meet network performance requirements. In this section, a dynamic TRP-side DTX method is proposed as a means to prevent TRPs from overheating. The proposed method imposes some restrictions on the transmission of slots in downlink, thus limiting the computational effort and power consumption/dissipation at TRP radio units, by dynamically changing the states of TRPs on a slot basis.

3.3.1 DTX states

Three TRP DTX states are defined:

- **A**ctive: When TRP $m \in \mathcal{M}$ has data activity with some UE. Then, $m \in \tilde{\mathcal{M}}$ and the TRP is *heating*.
- **I**nactive: When TRP $m \in \mathcal{M}$ has no data activity with any UE. Then, $m \in \tilde{\mathcal{M}}$, but the TRP is *cooling*.
- **S**leep: When TRP $m \in \mathcal{M}$ is switched off. Then, $m \notin \tilde{\mathcal{M}}$ and the TRP is *cooling*.

When a TRP enters a DTX sleep state, ongoing transmissions are interrupted, keeping assigned packets on a buffer.

Let $n_m^{\text{slot}} \in \mathbb{Z}^*$ be a slot counter implemented by TRP m, $\forall m \in \mathcal{M}$. A TRP m in DTX active state increments n_m^{slot} by one after transmitting a slot, while decrements it by one if that TRP is in either inactive or sleep state. States active and inactive mean that a TRP is *awake*; thus, it is available to transmit data to a UE. On the other hand, when in sleep mode, TRP m can only awaken after a back-off period $n_m^{\text{off}} \in \mathbb{Z}^*$.

The rationale behind the slot counting is to obtain a simple, linear model that approximates the TRP thermal behavior when heating/cooling, as illustrated in Fig. 7. Here, it takes longer for a TRP to cool down than to heat up. In this sense, $K^{\text{cool}} > 1$ denotes the number of slots needed to cool down to the temperature prior to a single slot transmission.

3.3.2 Slot counting constraints.

For a TRP m to change to sleep state, its slot counter n_m^{slot} must violate at least one out of two constraints C1 and C2. More specifically:

C1: As aforementioned, n_m^{slot} cannot exceed threshold $n^{\max}$; otherwise, TRP m starts suffering overheating issues and must be switched off, then staying in sleep mode during a back-off period $n_m^{\text{off}} = K^{\text{cool}}$ slots.

C2: TRPs needs to always be able to transmit SSs. Let n_m^{budget} be the slot budget available at slot j for TRP m to transmit n^{SS} consecutive slots conveying SSs in the next SS

Figure 7 – Dynamic DTX example showing the slot counter evolving over time. Here SS followed by data transmission are capped by cooling intervals due to C1, then a longer C2 cool-down period to be able to transmit the next SS burst.

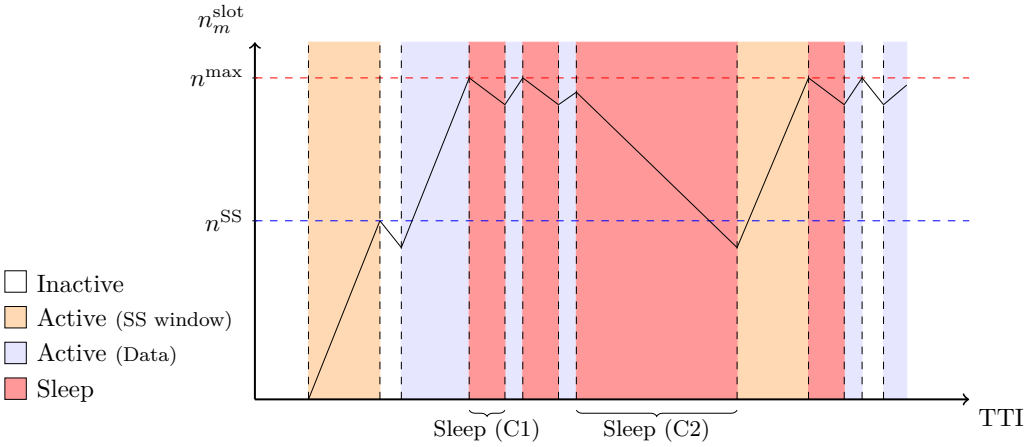

Source: Created by the author.

window T^{SS}, assuming no transmissions until then, defined as:

$$n_m^{\text{budget}} = \max\left(K^{\text{cool}} n_m^{\text{slot}} - \text{f}\left(j, T^{\text{SS}}\right), 0\right) + n^{\text{SS}}, \tag{3.8}$$

where $\text{f}(x,y) = y - (x \mod y)$ stands for the complementary modulus operation. To avoid overheating of TRP m, its n_m^{budget} cannot exceed threshold $n^{\max}$ at slot j; otherwise, TRP m will suffer overheating issues at the end of the next SS window, unless TRP m is switched off at slot j, then staying in sleep mode during a back-off period $n_m^{\text{off}} = K^{\text{cool}}\text{f}\left(j, T^{\text{SS}}\right)$ slots.

The main steps of the proposed TRP DTX method discussed above are described in Algorithm 3.1 and depicted on the flowchart in Fig. 8, which is executed by TRP m, $\forall m \in \mathcal{M}$, at slot j, to in turn obtain an updated subset $\tilde{\mathcal{M}}$ for the next slot.

3.4 System level aspects

The proposed TRP DTX method is assessed from a system-level perspective as the main objective in this chapter. To this end, Algorithm 3.1 described in Section 3.3 was incorporated into a system-level simulator to evaluate the performance of the system modeled in Section 3.2 under different DTX setups.

To provide a full scale system-level simulation, main aspects of 5G NR systems have been considered. The adopted system-level simulator implements i) beam-based transmissions via BM procedures, with ii) traffic model, and iii) UE scheduling. Also, different system-level metrics were calculated as key performance indicators (KPIs), namely UE throughput, SINR and the DTX states distribution. In the following subsections, each of the listed aspects will be discussed.

Algorithm 3.1 algorithm

Dynamic TRP DTX at slot j

for $m \in \mathcal{M}$ **do**
  if $n_m^{\text{off}} = 0$ **then** # TRP awake
    if $n_m^{\text{slot}} < n^{\max}$ **then** # C1
      if $n_m^{\text{budget}} < n^{\max}$ **then** # C2
        if Data activity **then**
          $n_m^{\text{slot}} \leftarrow n_m^{\text{slot}} + 1$ # Slot counter increased due to activity
        else # TRP inactive
          $n_m^{\text{slot}} \leftarrow \max\left(n_m^{\text{slot}} - 1, 0\right)$ # Slot counter decreased
        end if
      else # TRP on sleep state due to C2
        $\tilde{\mathcal{M}} \leftarrow \tilde{\mathcal{M}} \backslash \{m\}$ # Remove TRP m from the set of active TRPs
        $n_m^{\text{slot}} \leftarrow \max\left(n_m^{\text{slot}} - 1, 0\right)$
        $n_m^{\text{off}} \leftarrow K^{\text{cool}} \mathrm{f}\left(j, T^{\text{SS}}\right) - 1$ # Set back-off period acording to C2
      end if
    else # TRP on sleep state due to C1
      $\tilde{\mathcal{M}} \leftarrow \tilde{\mathcal{M}} \backslash \{m\}$
      $n_m^{\text{slot}} \leftarrow \max\left(n_m^{\text{slot}} - 1, 0\right)$
      $n_m^{\text{off}} \leftarrow K^{\text{cool}}$ # Set back-off period acording to C1
    end if
  else # TRP back-off count update
    $n_m^{\text{slot}} \leftarrow \max\left(n_m^{\text{slot}} - 1, 0\right)$
    $n_m^{\text{off}} \leftarrow n_m^{\text{off}} - 1$
    if $n_m^{\text{off}} = 0$ **then** # TRP awakes
      $\tilde{\mathcal{M}} \leftarrow \tilde{\mathcal{M}} \cup \{m\}$ # Update the set of available TRPs
    end if
  end if # Update SS slot budget
  $n_m^{\text{budget}} \leftarrow \max\left(K^{\text{cool}} n_m^{\text{slot}} - \mathrm{f}\left(j, T^{\text{SS}}\right), 0\right) + n^{\text{SS}}$
end for

3.4.1 Beam management

The beam management has the goal of maintaining BPLs between TRPs and connected UE panels by compensating the channel dynamics along time and thus keeping a suitable beam alignment as the UE moves around. For idle UEs, BM has the task of providing initial access through a directional BPL, which allows the UE to establish its first access to the network.

As for the the beam management framework considered in this chapter, it has been assumed that all UEs are connected all the time. The UE only has one active panel at a time, hence, for each UE the beam management only execute procedures for the active panel.

3.4.1.1 Beam sweeping

The adopted beam management framework has the goal of finding at least one BPL for each UE panel by exploring angular regions to identify more suitable analog beams. This exploration is made by the beam sweeping procedures that can be executed at TRP and/or UE

Figure 8 – Dynamic DTX flowchart for the steps in Algorithm 3.1.

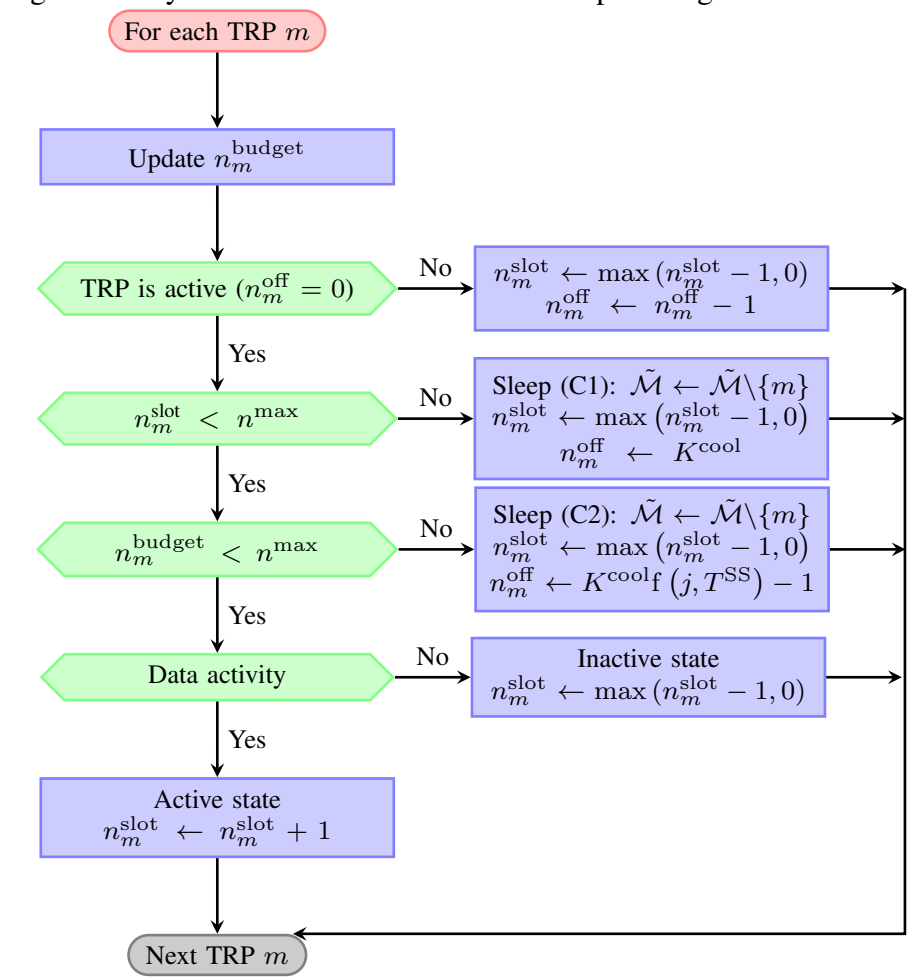

Source: Created by the author.

side as described below:

- Procedure 1 (P1): TRP and UE beam sweeping of wide analog beams. This procedure is used for the identification of a new angular region for connected UEs.
- Procedure 2 (P2): TRP beam sweeping only. This procedure is the refinement of BPL at TRP side. Narrow beams are swept into the angular coverage of the best TRP wide analog beam detected during P1. It is executed only for connected UEs, whose beams are kept fixed.
- Procedure 3 (P3): Connected UEs beam sweeping only. This procedure is the refinement of BPL at the UE side. This sweeping is made considering narrow beams into the angular region of the wide analog beam at UE side identified during P1.

In P1, a block of $L^{\text{P1}} = 256$ SSs is transmitted by the TRPs sweeping a sequence of wide beams, pointing to different directions as a means to entirely illuminate its coverage area, within a 5-ms window for the UE to measure their RSRP, while the UE beam, herein assumed a wide beam, is kept fixed. This procedure represents the P1 beam sweeping, and it is repeated with a periodicity of $T^{\text{SS}} = 20$ ms, as illustrated in Fig. 9. In turn, the UE reports to the TRP

Figure 9 – SS burst set.

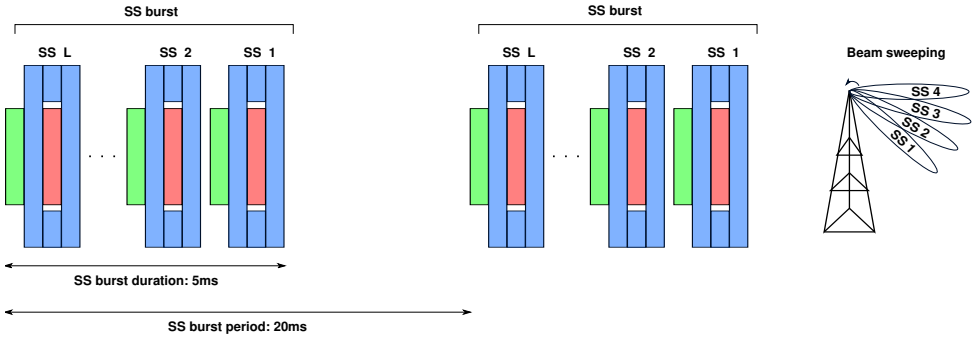

Source: Created by the author.

Figure 10 – Beam management events over time.

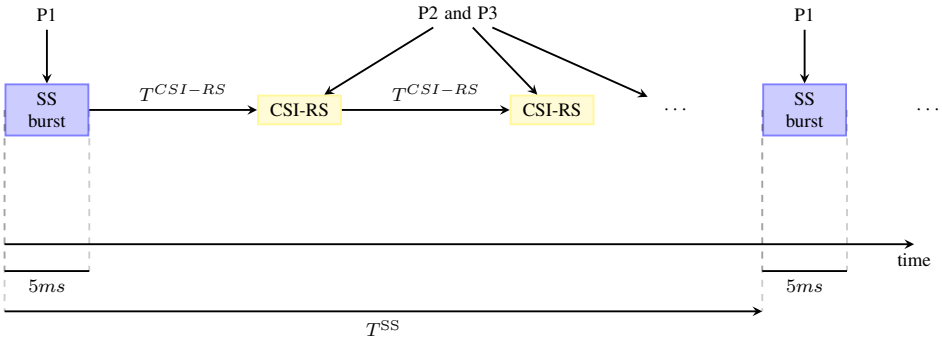

Source: Created by the author.

which transmitted SS was measured with highest RSRP. It is worth mentioning that only two SS blocks can be transmitted during a single time slot.

For the refinement in P2, CSI-RSs are transmitted in the period between SS blocks with periodicity $T^{\text{CSI-RS}}$. The TRP sweeps $L^{\text{P2}} = 8$ narrow beams within the angular space of the wide beam selected in a previous P1, in bursts of 4 beams with an offset of 5 slots to boost the beamforming gain towards the UE. The TRP then uses such knowledge to select the beam for subsequent transmissions, while the UE keeps its current beam.

Finally, in P3, the goal is to adjust the UE beam. To this end, the TRP repeatedly uses the beam selected in P2 for L^{P3} CSI-RS transmissions, for the UE to measure RSRP, while sweeping $L^{\text{P3}} = 4$ narrow beams pointing to different directions. In turn, the UE selects the best beam in terms of RSRP in (3.6) for subsequent transmissions. Note that P2 and P3 depend on P1; thus, they take place after the P1 5-millisecond window. In case multiple UEs are connected to the same TRP, it performs P2 and P3 for each UE in a round-robin fashion. In Fig. 10, a representation of beam sweeping of the BM framework considered in the system-level simulations is presented.

Since every wide beam overlaps a subset of narrow beams, a mapping between wide and narrow beams is established to speed up P2 and P3. To this end, each TRP wide beam in $\mathcal{A}_{N_t,2}$ is mapped onto the L^{P2} TRP best narrow beams in $\mathcal{B}_{N_t,2}$ in terms of inner product. Analogously, each UE wide beam in $\mathcal{A}_{N_r,1}$ is mapped onto the L^{P3} UE best narrow beams in $\mathcal{B}_{N_r,1}$.

3.4.1.2 Panel switching

In the scenario assessed in this chapter, a UE panel switch feature is also enabled, which provides additional diversity to the system to be explored. By this feature UEs explore their multiple panels by running P1 always with a different panel in a round-robin fashion to sound candidate BPLs from TRPs in subset $\tilde{\mathcal{M}}$. They switch panels for subsequent data activity only if a better BPL of wide beams than that selected in a previous P1, in terms of RSRP in (3.6), is found.

3.4.1.3 Beam recovery

Another important aspect of BM is the beam recovery process. Here, a beam failure event happens when no CSI-RS is detected during P2 after a UE-panel and TRP-panel lose the BPL connection. Such a sudden event may be caused by a blockage, or due to fast UE mobility. It then triggers the beam recovery procedure which consists of waiting for the next SS window to establish a new BPL, assuming that the UE will use its wide beam found in the previous P1. It is worth mentioning that if a TRP status needs to be set to sleep by the DTX, no sounding or recovery process is triggered. The scheduler will search for another BPL candidate for transmissions or – if no beam pair is available – it will wait until the next SS window for the BM procedures restarting from P1.

3.4.2 Traffic model

In order to simulate data for the system-level simulations performed in this chapter, a packet-based traffic model has been considered for all UEs. It generates a packet containing R_{pkt} bits within the period of T_{pkt} seconds. At the beginning of the simulation, the first packet of the k-th UE is generated after a random period of τ_{pkt} multiple of the simulation time step, and then the subsequent packets arrive at the buffer periodically with period T_{pkt}. For simplicity, R_{pkt} and T_{pkt} are fixed; thus, the UE traffic generation during the simulation is constant, herein referred to as *Fixed Periodic* traffic.

Also, an infinite transmitter buffer is adopted and generated packets do not expire. Similar to the scheduler and BBU, we assume that the transmitter buffer is centralized. In this way, the packets to be transmitted will be available at each one of the TRPs in the coordination cluster.

Despite the static parameters of packet generation per UE, the traffic demand per TRP can vary with the number of associated UEs. Therefore, along the same simulation, the traffic demand of a given TRP may vary in consequence of beam management procedures, since the UE-TRP association in the cluster can vary with BPL quality and with the DTX regime.

3.4.3 Evaluation metrics

As for the system-level metrics considered in this work, the SINR has been defined in Section 3.2 and is used to calculate UE's throughput in accordance with the physical layer abstraction, the mapping from SINR to transmit data rate, which is based on modulation and coding schemes (MCSs).

In order to analyze the effective throughput in a transmission, it is necessary to consider the BLER, defined as the ratio between the number of blocks received with error and the total number of transmitted blocks.

Assuming a target BLER of 10% and considering that in a given slot j, the b-th panel of UE k received data in RB q using the MCS [5] υ, the number of received bits is given by:

$$B_{k,b}[q,j] = \min\left(|\mathcal{S}_j^{\text{data}}|B_\upsilon \text{BLER}\left(\upsilon, \gamma_{k,b,m}[q,j]\right), R_k^{\text{buffer}}\right), \tag{3.9}$$

where R_k^{buffer} is the number of bits in the transmitter buffer for UE k, B_υ is the number of bits that MCS υ can transmit in a single RB, and $\text{BLER}(\upsilon, \gamma_{k,b,m}[q,j])$ is a random process that maps the SINR from (3.7) for the MCS υ into a binary value. The random process $\text{BLER}\left(\upsilon, \gamma_{k,b,m}[q,j]\right)$ is modeled as a uniform variable $\mathcal{U}(0,1)$ in slot j.

For each transmission, a uniform variable sample is calculated, so that if the value is lower than the probability of error in MCS υ and SINR $\gamma_{k,b,m}[q,j]$ it returns 0; otherwise, the outcome is 1. Finally, for each UE k at slot j, its throughput is:

$$r_{k,j} = \frac{\sum_{b=1}^{4}\sum_{q=1}^{Q}\sum_{\bar{j}=1}^{j} B_{k,b}[q,\bar{j}]}{t_{\text{slot}}\sum_{\bar{j}=1}^{j}\bar{\lambda}_{k,b}[q,\bar{j}]}, \tag{3.10}$$

where t_{slot} is the slot duration in seconds and $\bar{\lambda}_{k,b}[q,j]$ is a binary variable indicating if R_k^{buffer} is empty at slot j.

Additionally, once a packet is generated to a UE, its latency is measured as the time elapsed from its generation instant until it is successfully received by that UE.

3.4.4 Scheduler

For transmission coordination a channel-aware multi-TRP scheduling in a TDM fashion has been adopted. It relies on SINR estimates to set transmission parameters, such as link adaptation, before every transmission. The SINR estimates are also used by the scheduler to decide which UE panel will be selected to receive data.

For simplicity, the equivalent channel in (3.1) is assumed to be perfectly known at TRPs. Hence, the SINR estimation has been defined as a linear average of the actual SINR values

[5] This work adopts an LTE-like link-to-system mapping [33].

until the slot of interest j as follows:

$$\bar{\gamma}_{k,b,m}[q,j] = \frac{\sum_{\bar{j}=1}^{j} \gamma_{k,b,m}[q,\bar{j}]}{j}. \tag{3.11}$$

The estimated SINR in (3.11) was used by the scheduler to decide which UE panel will be allocated with RBs in a given TTI and also which MCS the link adaptation should select to its transmission. In cases that the SINR threshold is below the BLER target of the smallest MCS level, the scheduler will not transmit within this RB.

During each TTI j, only one UE panel is served by one TRP panel using the entire bandwidth and based on fairness utility defined as

$$u_{m,k,b}[j] = \frac{\bar{r}_{m,k,b}}{r_k[j]}, \tag{3.12}$$

where $r_k[j]$ is the throughput of UE k in TTI j calculated using (3.10) and $\bar{r}_{m,k,b}$ is the expected throughput of UE k in the current TTI j if the UE panel (k,b) has been scheduled to the RBs of the TRP that is estimated applying the estimated SINR in (3.11) into (3.10).

Defining $\mathcal{S}_m$ as a set containing the UE panel candidates to be scheduled by the TRP m, the multi-TRP scheduling is described in Algorithm 3.2.

Algorithm 3.2 Multi-TRP scheduling algorithm for a TTI j.

1: Define $\Lambda_{k,b,j} = 0 \quad \forall k$ and $\forall b$.
2: **for** each TRP m **do**
3: Schedule all RBs of TRP m for the UE-panel that: $k^*, b^* = \underset{\forall (k,b) \in \mathcal{S}_m}{\arg\max} \left\{ u_{m,k,b} \right\}$.
4: Update $r_{k^*}[j] \leftarrow \bar{r}_{m,k^*,b^*}$.
5: Update $\Lambda_{k^*,b^*}[j] \leftarrow 1$.
6: Remove $\mathcal{S}_{\bar{m}} \leftarrow k^*, b^* \setminus \mathcal{S}_{\bar{m}} \; \forall \bar{m}$
7: **end for**

In the first step, the allocation variables $\Lambda_{k,b}[j]$ are defined as zero. The loop between Step 2 and Step 7 sequentially allocates all RBs for each TRP panel in the cluster to the UE panel that has the largest fairness utility. After one TRP panel defines the scheduled UE panel, the throughput of the selected UE is updated considering that this transmission will be successful. At the end of loop, the scheduled UE panels are removed from all $\mathcal{S}_{\bar{m}}$ in order to guarantee that this UE panel will not receive data using this same panel.

The main goal of the scheduling algorithm is to achieve fairness among UEs associated with the same TRP. In general, this goal is not feasible since the UE may receive data from two different TRPs. Note that the proposed algorithm can lead to situations where each panel of the same UE is served by a different TRP-panel, and thus a non-coherent (NC)-joint transmission (JT) transmission.

3.5 Simulation results

In this section, the numerical results regarding the impact of employing the DTX framework described in Section 3.3 in a system-level simulator is presented and discussed. First, the general simulation setup will be detailed.

The channel model in (3.1) is configured as line-of-sight (LOS)-only urban micro (UMi) O2O scenario [28], with intersite distance (ISD) of 100 m, where outdoor UEs are randomly dropped inside the hotspot region depicted in Fig. 6 with height of 1.5 m and move at 3 km/h following a uniformly-distributed random direction on the xy plane. The coordination cluster contains 3 TRPs with height of 10 m, $P_{\text{TX}} = 33$ dBm, $\sigma_n^2 = -174$ dBm/Hz, and $L^{\text{SS}} = 256$ SSs. Once dropped, every UE randomly chooses one panel and initially selects the corresponding "main-lobe" beam from that panel to establish a BPL during the first P1.

Each TRP has a 16×16 URA, while each UE has four 16×4 URA panels oriented perpendicularly to the xy-plane, each pointing to a different UE side (left, right, front and back), with random rotation around the z-axis. A complete summary of the general simulation parameters is presented in Table 5.

As for the DTX setup, two threshold $n^{\max}$ values are considered: a) 640 slots for the baseline, and b) 320 slots as a more aggressive restriction. $K^{\text{cool}} = 2$ indicating that the amount of slots needed to cool down the temperature is twice as the slot duration.

For the traffic generation it has been assumed that all UEs have Fixed Periodic Traffic model, as described in Section 3.4.2, with packets containing $R_{\text{pkt}} = 0.5$ Mbytes within the period of $T_{\text{pkt}} = 16$ ms or $T_{\text{pkt}} = 8$ ms for a higher load scenario.

For the sake of comparison, a baseline mmWave system is considered, which, in general, has the same parameter setting as the THz in Table 5 except for the specific parameters listed in Table 6 for each scenario. The goal is to evaluate the impact of the proposed DTX on the system performance. 250 Monte Carlo runs have been simulated for each approach considering a simulation time of 1 s, but only accounting for the last 100 ms of KPI measurements in order to avoid transient effects. The results were gathered at the end of a simulate slot. As they demand the whole simulation chain to carry out system-level evaluations, the simulation runs performed to generate such results faced significant computational complexity issues, given the simulated scenario presented in Section 3.2.

In summary, the cases considered for the system performance evaluation are listed as follows:

- mmWave - $T_{\text{pkt}} = 16$ ms: Baseline case for comparison with respect to the shift to higher frequency bands;
- mmWave - $T_{\text{pkt}} = 8$ ms: Baseline case considering shorter packet generation period;
- THz - $T_{\text{pkt}} = 16$ ms: Scenario considering THz bands and traffic periodicity of 16 ms. It is the baseline scenario to compare with the DTX setups;

Table 5 – General simulation parameters.

Scenario	UMi: O2O [28] (LOS)
TRP height	10 m
Downlink total transmit power (per TRP)	33 dBm
Outdoor UE drop	Uniform within the coord. cluster hotspot
UE height	1.5 m
ISD	100 m
Channel model	5G stochastic radio channel for dual mobility (5G-StoRM) [27]
Space-time consistency	Procedure B [28]
Blockage	Stochastic blockage model A [28] and panel blockage
Antenna element type (for both TRP and UE)	Dual polarized, radiation pattern according to [28]
Antenna panel type (for both TRP and UE)	URA ($\lambda/2$ element spacing, single RF chain per polarization)
Num. TRP panels	1
Num. UE panels	4 (left, right, front and back – one active at time)
UE speed	3 km/h
TRP panel beam codebook	DFT with oversampling factor of 2 (wide and narrow beams)
UE panel beam codebook	DFT with oversampling factor of 1
$T^{\text{CSI-RS}}$	5 slots
T^{SS}	20 ms
RSRP threshold	−140 dBm
Scheduler	TDM, proportional fairness
MCS mapping	LTE-A-like according to 3GPP TR 36.213 [34]
R_{pkt}	0.5 Mbytes (4096000 bits)
T_{pkt}	16 ms and 8 ms
Monte Carlo samples	250
Simulation time	1 s
Num. UEs in each sector	1
UE panel switch mode	Round-robin

Source: Created by the author.

Table 6 – Key simulation parameters.

	mmWave	THz
Carrier frequency f_c	28 GHz	100 GHz
Subcarrier spacing L_{sc}	120 kHz	960 kHz
TRP URA $(N_t/2 \times N_t/2)$	8×8	16×16
UE URA $(N_r/2 \times N_r/2)$	8×2	16×4
N. of TRP wide beams $\lvert\mathcal{A}_{N_t,2}\rvert$	64	256
N. of UE wide beams $\lvert\mathcal{A}_{N_r,1}\rvert$	4	16
Bandwidth L_{BW}	400 MHz	3.04 GHz
Slot duration $t_{\text{slot}} = 1/N_{\text{slot}}$	1/8 ms	1/64 ms

Source: Created by the author.

- THz - T_{pkt} = 8 ms: THz scenario with double packet generation rate;
- DTX(1) - T_{pkt} = 16 ms: First DTX configuration case, with $n^{\max}$ = 640;
- DTX(1) - T_{pkt} = 8 ms: First DTX configuration with double packet generation rate;
- DTX(2) - T_{pkt} = 16 ms: More aggressive DTX configuration case, with $n^{\max}$ = 320;
- DTX(2) - T_{pkt} = 8ms: Aggressive DTX configuration, considering double packet generation rate;

Figure 11 – CDF of UE throughput. DTX(1) and DTX(2) represent the $n^{\max}$ values of 640 and 320, respectively.

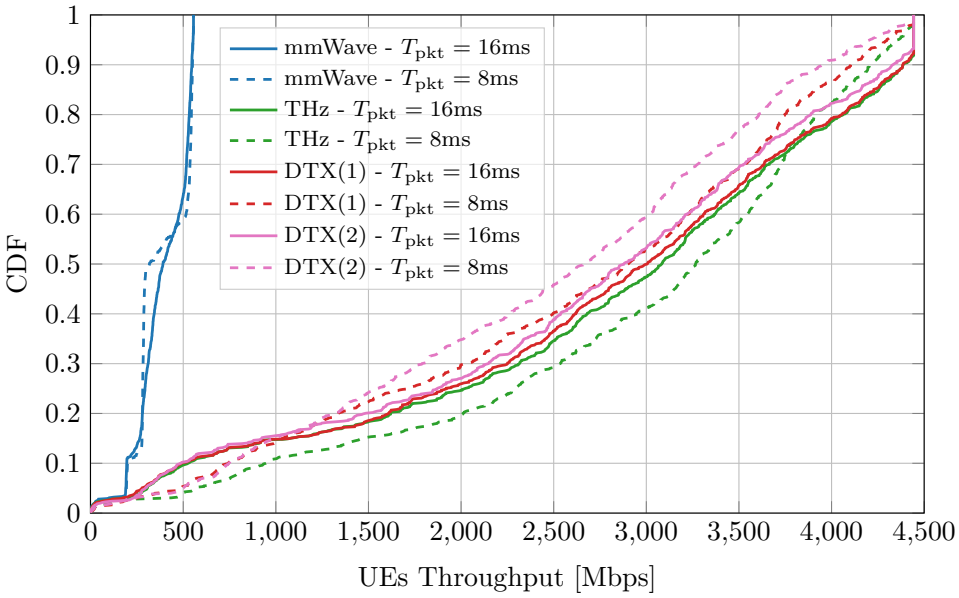

Source: Created by the author.

Fig. 11 shows the cumulative distribution function (CDF) of the UE throughput in (3.10) for the different setups. In general, the slot counting constraints described in Sec. 3.3 contribute to a UE throughput degradation because TRPs are switched off even if their buffers have data to deliver. For instance, throughput losses of approximately 2.56% and 6.65% at the 50th percentile were observed by deploying DTX in the THz system for T_{pkt} of 16 ms considering $n^{\max} = 640$ and $n^{\max} = 320$, respectively. As for the higher traffic with T_{pkt} of 8ms, losses of approximately 11.18% and 18.35% were observed.

The larger throughput loss in the higher traffic load case when DTX is used is explained by the fact that DTX sleep states occur more often, the same behavior is present when varying the maximum threshold $n^{\max}$.

On the other hand, in comparison with the baseline, the THz system with more aggressive DTX in the higher traffic load case reached about 6.84 times more throughput. Thus, even with the throughput losses caused by DTX, the wider L_{BW} in the THz band still strongly contributes to the high UE throughput gain observed, which *per se* can justify shifting f_c towards THz bands.

Fig. 12 shows the CDF of the mean SINR, by averaging (3.7) over RBs allocated to scheduled UEs, for each case. Clearly, the THz system experienced an SINR degradation when compared to the baseline mmWave system of about 5.6 dB at the 50th percentile. Although larger achievable beamforming gains could compensate i) higher noise power due to the wider L_{BW}, and ii) higher propagation losses, narrower beams at both ends lead to higher spatial misalignment, then reducing the experienced beamforming gain.

Fig. 13 shows the impact on the system performance when UE panels are switched by comparing the CDF of the available BPLs RSRP for each UE. It is possible to observe that the

Figure 12 – CDF of SINR for each simulated case. DTX(1) and DTX(2) represent the $n^{\max}$ values of 640 and 320, respectively.

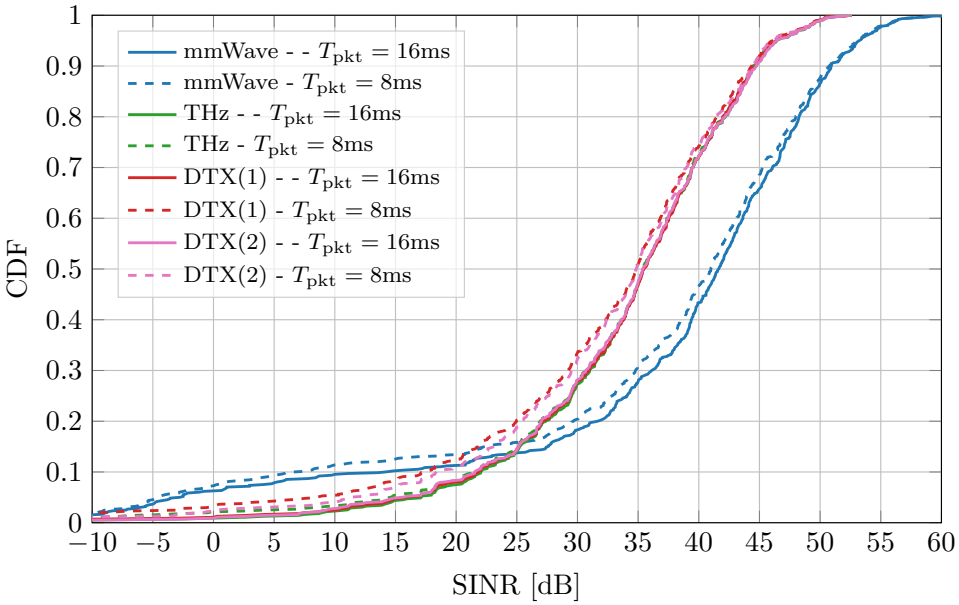

Source: Created by the author.

Figure 13 – CDF of the RSRP of the available BPL for all UEs within the 100ms window.

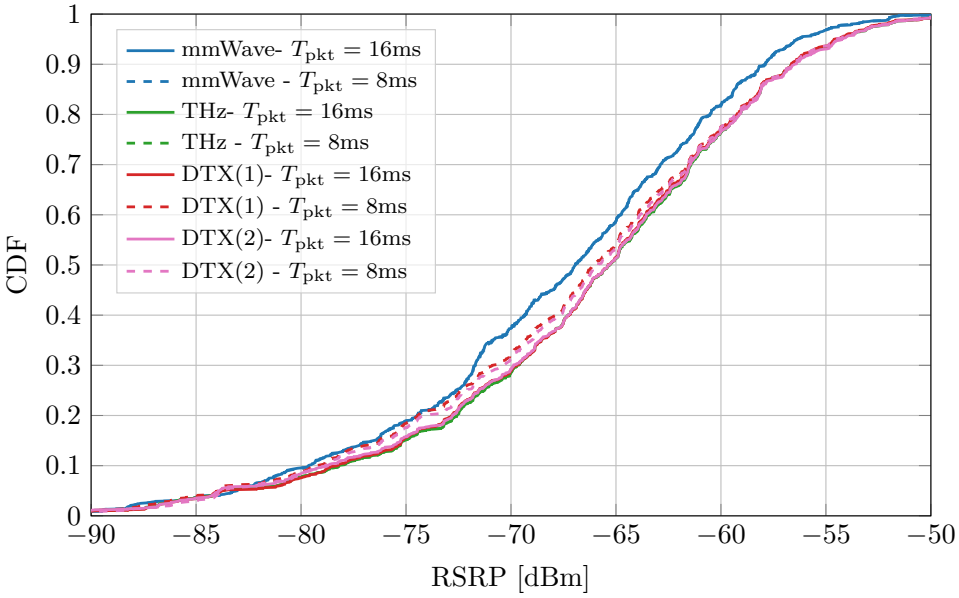

Source: Created by the author.

achievable array gain by increasing both the TRP and UE panel size as described in Table. 6 when shifting frequency bands from mmWave to THz, and exploring the available UE panels provided a difference of approximately 2 dB at the 50th percentile. Thus, indicating that exploring panel diversity might improve the RSRP levels regarding the higher propagation losses in the sub-THz environment.

Additionally, in Table. 7 the average packet latency considering all packets transmitted during the considered 100 ms window is presented for each case. It is possible to see that

Table 7 – Average packet latency.

Case	Avg pkt latency
mmWave - T_{pkt} = 16ms	1.077×10^{-2}
THz - T_{pkt} = 16ms	2.072×10^{-3}
DTX (1) - T_{pkt} = 16ms	2.250×10^{-3}
DTX (2) - T_{pkt} = 16ms	2.314×10^{-3}
mmWave - T_{pkt} = 8ms	9.382×10^{-3}
THz - T_{pkt} = 8ms	1.807×10^{-3}
DTX (1) - T_{pkt} = 8ms	2.998×10^{-3}
DTX (2) - T_{pkt} = 8ms	2.835×10^{-3}

Source: Created by the author.

Table 8 – DTX states ratio for each simulated case.

Case	Active	Inactive	Sleep
mmWave - T_{pkt} = 16ms	55.73	44.27	–
THz - T_{pkt} = 16ms	15.58	84.42	–
DTX (1) - T_{pkt} = 16ms	15.39	84.30	0.31
DTX (2) - T_{pkt} = 16ms	15.47	84.10	0.43
mmWave - T_{pkt} = 8ms	74.39	25.61	–
THz - T_{pkt} = 8ms	21.19	78.81	–
DTX (1) - T_{pkt} = 8ms	21.00	76.72	2.28
DTX (2) - T_{pkt} = 8ms	20.78	76.70	2.52

Source: Created by the author.

under DTX the system experienced more latency for both traffic configurations. The mmWave setup achieved the highest values, behavior related to the lower throughput achieved.

Finally, Table. 8 presents the average of the DTX state ratio for all TRPs. This ratio was computed considering the last 100 ms of the simulation time. It is possible to see that the percentage of the sleep states are below 3%, with the TRPs spending the most of the time inactive for the majority of the simulated scenarios. This behavior indicates that overall system load is supported by the THz setup. Nevertheless, the increase in data traffic by changing T_{pkt} contributes to the increase of the TRP activity and, hence, for increasing the sleep states.

The states distribution impact on system performance can be noticed on the SINR and throughput CDFs presented in Fig. 12 and Fig. 11, with more activity leading to more data transmission and thus higher perceived interference.

3.6 Chapter summary

This chapter presented system-level evaluations of a THz system in a LOS-only UMi scenario with outdoor UEs within a 3-TRP coordination cluster. TRP-side DTX is proposed to avoid overheating of TRP's radio units. Numerical results have shown that a large throughput gain can be achieved when shifting from a baseline mmWave band to the THz one, despite the DTX dynamics. On the other hand, the THz system experienced an SINR degradation as the provided beamforming gain was not enough to compensate for larger propagation losses and larger noise power. As expected, DTX leads to throughput reduction, but further analysis can

provide better understanding regarding the impact of this strategy on other KPIs.

4 CONCLUSIONS

In the context of the evolution of mobile communication systems, the optimization and development of new technologies are essential to meet the demand and requirements of new application scenarios. This work addressed two distinct scenarios of mobile communication systems, both considering a specific problem involving aspects of 5G and 6G systems.

In **Chapter 2** a 5G scenario was considered. It has assessed the performance of a DNN BF strategy for a MU-MISO system and provided a robustness analysis regarding ICSI. The main goal was the maximization of the weighted sum rate, which is by definition a non-convex problem whose parameterized optimal solution is hard to be obtained.

A DNN BF strategy was applied in order to obtain a suboptimal solution with reduced complexity. The learning model considered is drawn from a DNN whose input is the channel response and output is the beamforming vector parameters, which are used to build the optimum beamforming vectors for all UEs. The WMMSE BF was considered for the comparison, and its parameters were used for the data generation and the supervised training of the DNN.

From the obtained results it was possible to verify that the deep learning based beamforming solution is viable and as robust as the WMMSE, where the channel estimation error has caused a similar effect on the average sum rate achieved for both solutions assuming that the channel and ICSI models follow the same distribution. Regarding the overall sum rate performance, the DNN approximates the WMMSE as much as possible due to its supervised nature, but its performance is bounded by the WMMSE BF and the WMMSE initialization. At last, the DNN BF applied after an offline training presented a reduced computational performance in comparison with the iterative solution, which, when considering its sum rate performance, ensures the DNN BF as a suitable strategy.

As perspectives for future works in this topic, one can consider an analysis applying other ICSI models with different statistical distributions, as well as consider more realistic channel models. Another interesting extension is the employment of DNN beamforming in a system considering multi-antenna UEs with multiple streams. Also, other learning approaches that can take use of the sum rate information as a reward, such as in reinforcement learning, could be pursued.

In **Chapter 3**, system-level simulations of a 6G scenario were considered. The scenario consisted of a system operating at 100 GHz in a LOS-only UMi scenario composed of a 3-TRP coordination cluster providing network access for outdoor multi-panel UEs under centralized beam management and scheduling. The impact of TRP overheating when operating in THz bands was considered and a TRP-side dynamic DTX was proposed, controlling the amount of slots a TRP can transmit continuously. Numerical results comparing the network performance of THz system in comparison with a mmWave setup and THz system under different DTX configurations were presented for two traffic load conditions.

The presented simulation results have shown that when shifting f_c from 28 to 100 GHz a throughput gain of at least 6.84 times could be achieved due to the wide bandwidth available, despite the DTX dynamics. The THz systems have a significant SINR degradation as the experienced beamforming gain was not enough to compensate for larger propagation losses and larger noise power. Nevertheless, the UE panel diversity provided by executing the BM procedure 1 with different panels in a round-robin fashion made it possible to improve the RSRP levels of the THz system above the mmWave, despite the higher propagation losses.

As expected, DTX leads to throughput reduction as the traffic load increases or with more aggressive setups due to the increase of sleep states events, but further analysis is needed to provide a better understanding regarding the impact of DTX on other KPIs, since the considered traffic setup did not stress the system enough to increase the ratio of sleep events considerably.

Also, as future works, one may consider larger URAs in the system, along with further optimization of the BM procedures, to potentially improve the experienced beamforming gains. In order to improve the dynamic DTX framework, a traffic aware approach may be considered as well.

REFERENCES

1 DAHLMAN, E.; PARKVALL, S.; SKÖLD, J. **5G NR**: the next generation wireless access technology. 1. ed. USA: Academic Press, Inc., 2018. ISBN 0128143231.

2 OSSEIRAN, A. et al. **5G wireless access: an overview**. 2020. Available from: <https://www.ericsson.com/en/reports-and-papers/white-papers/5g-wireless-access-an-overview>. Accessed on: 28 Aug. 2023.

3 SANTANA JR., E. de et al. On the robustness of deep learning based beamforming for MU-MISO systems. *In*: SIMPÓSIO BRASILEIRO DE TELECOMUNICAÇÕES E PROCESSAMENTO DE SINAIS (SBrT2021), XXXIX., 2021, Fortaleza. **Anais** [...]. Rio de Janeiro: Sociedade Brasileira de Telecomunicações, 2021. p. 1–5. DOI: 10.14209/sbrt.2021.1570730492.

4 BUTOVITSCH, P. von et al. **Advanced antenna systems for 5G networks**. 2018. Available from: <https://www.ericsson.com/en/reports-and-papers/white-papers/advanced-antenna-systems-for-5g-networks>. Accessed on: 28 Aug. 2023.

5 CHRISTENSEN, S. S. et al. Weighted sum-rate maximization using weighted MMSE for MIMO-BC beamforming design. **IEEE Transactions on Wireless Communications**, [S.l.], v. 7, n. 12, p. 4792–4799, dec. 2008. DOI: 10.1109/T-WC.2008.070851.

6 LUO, F.-L. **Machine learning for future wireless communications**. 1. ed. [S.l.]: Wiley-IEEE Press, 2020. DOI: 10.1002/9781119562306.

7 SUN, H. et al. Learning to optimize: training deep neural networks for interference management. **IEEE Transactions on Signal Processing**, [S.l.], v. 66, n. 20, p. 5438–5453, oct. 2018. ISSN 1941-0476. DOI: 10.1109/tsp.2018.2866382.

8 XIA, W. et al. A deep learning framework for optimization of MISO downlink beamforming. **IEEE Transactions on Communications**, [S.l.], v. 68, n. 3, p. 1866–1880, mar. 2020. DOI: 10.1109/TCOMM.2019.2960361.

9 ALEXANDROPOULOS, G. C.; FERRAND, P.; PAPADIAS, C. B. On the robustness of coordinated beamforming to uncoordinated interference and CSI uncertainty. *In*: 2017 IEEE WIRELESS COMMUNICATIONS AND NETWORKING CONFERENCE (WCNC), 2017, San Francisco. **Proceedings** [...]. New York: IEEE, 2017. p. 1–6. DOI: doi:10.1109/WCNC.2017.7925853.

10 BRAGA, I. M. et al. User scheduling based on multi-agent deep Q-learning for robust beamforming in multicell MISO systems. **IEEE Communications Letters**, [S.l.], v. 24, n. 12, p. 2809–2813, dec. 2020. DOI: 10.1109/LCOMM.2020.3015462.

11 RUSEK, F. et al. Scaling up MIMO: opportunities and challenges with very large arrays. **IEEE Signal Processing Magazine**, [S.l.], v. 30, n. 1, p. 40–60, jan. 2013. DOI: 10.1109/MSP.2011.2178495.

12 MI, D. et al. Massive MIMO performance with imperfect channel reciprocity and channel estimation error. **IEEE Transactions on Communications**, [S.l.], v. 65, n. 9, p. 3734–3749, sept. 2017. DOI: 10.1109/TCOMM.2017.2676088.

13 BJÖRNSON, E.; BENGTSSON, M.; OTTERSTEN, B. Optimal multiuser transmit beamforming: a difficult problem with a simple solution structure [lecture notes]. **IEEE Signal Processing Magazine**, [S.l.], v. 31, n. 4, p. 142–148, july 2014. DOI: 10.1109/MSP.2014.2312183.

14 BJÖRNSON, E.; JORSWIECK, E., et al. Optimal resource allocation in coordinated multi-cell systems. **Foundations and Trends® in Communications and Information Theory**, [S.l.], v. 9, n. 2–3, p. 113–381, 2013. ISSN 1567-2190. DOI: 10.1561/0100000069.

15 SHI, Q. et al. An iteratively weighted MMSE approach to distributed sum-utility maximization for a MIMO interfering broadcast channel. **IEEE Transactions on Signal Processing**, [S.l.], v. 59, n. 9, p. 4331–4340, sept. 2011. DOI: 10.1109/TSP.2011.2147784.

16 3GPP. **TR 36.942:** Evolved Universal Terrestrial Radio Access (E-UTRA); Radio Frequency (RF) system scenarios. Technical report. [S.l.], 2020.

17 AKYILDIZ, I. F.; JORNET, J. M.; HAN, C. Terahertz band: next frontier for wireless communications. **Physical Communication**, [S.l.], v. 12, p. 16–32, 2014. ISSN 1874-4907. DOI: https://doi.org/10.1016/j.phycom.2014.01.006.

18 HAN, C.; AKYILDIZ, I. F. Distance-aware bandwidth-adaptive resource allocation for wireless systems in the terahertz band. **IEEE Transactions on Terahertz Science and Technology**, [S.l.], v. 6, n. 4, p. 541–553, 2016. DOI: 10.1109/TTHZ.2016.2569460.

19 BUTOVITSCH, P. von et al. **Advanced antenna systems for 5G networks**. 2018.

20 3GPP. **TS 38.214: Physical layer procedures for data**. report. [S.l.], 2018.

21 ASTELY, D. et al. **Meeting 5G network requirements with Massive MIMO**. 2022.

22 YANG, H.; MARZETTA, T. L. Total energy efficiency of cellular large scale antenna system multiple access mobile networks. *In*: 2013 IEEE ONLINE CONFERENCE ON GREEN COMMUNICATIONS (OnlineGreenComm), 2013, Piscataway. **Proceedings** [...]. New York: IEEE, 2013. p. 27–32. DOI: 10.1109/OnlineGreenCom.2013.6731024.

23 DUTTA, S. et al. A Case for Digital Beamforming at mmWave. **IEEE Transactions on Wireless Communications**, [S.l.], v. 19, n. 2, p. 756–770, 2020. DOI: 10.1109/TWC.2019.2948329.

24 ALI SHAH, S. H. et al. Power efficient discontinuous reception in THz and mmWave wireless systems. *In*: 2019 IEEE 20th INTERNATIONAL WORKSHOP ON SIGNAL PROCESSING ADVANCES IN WIRELESS COMMUNICATIONS (SPAWC), 2019, Cannes. **Proceedings** [. . .]. New York: IEEE, 2019. p. 1–5. DOI: 10.1109/SPAWC.2019.8815451.

25 FRENGER, P.; TANO, R. More capacity and less power: how 5G NR can reduce network energy consumption. *In*: 2019 IEEE 89th VEHICULAR TECHNOLOGY CONFERENCE (VTC2019-Spring), 2019, Kuala Lumpur. **Proceedings** [. . .]. New York: IEEE, 2019. p. 1–5. DOI: 10.1109/VTCSpring.2019.8746600.

26 CHOI, M. et al. Cell on/off parameter optimization for saving energy via reinforcement learning. *In*: 2021 IEEE GLOBECOM WORKSHOPS (GC Wkshps), 2021, Madrid. **Proceedings** [. . .]. New York: IEEE, 2021. p. 1–6. DOI: 10.1109/GCWkshps52748.2021.9682160.

27 PESSOA, A. M. et al. A Stochastic Channel Model With Dual Mobility for 5G Massive Networks. **IEEE Access**, v. 7, p. 149971–149987, 2019. DOI: 10.1109/ACCESS.2019.2947407.

28 3GPP. **TR 38.901**: study on channel model for frequencies from 0.5 to 100 GHz. Technical report. [S.l.], 2019.

29 PESSOA, A. M. et al. A spatially sonsistent Gaussian process for dual mobility in the 3D space. **IEEE Wireless Communications Letters**, [S.l.], v. 9, n. 11, p. 1803–1807, 2020. DOI: 10.1109/LWC.2020.2992725.

30 PESSOA, A. M. et al. A positive semidefinite autocorrelation function for modeling 3D Gaussian processes. **IEEE Transactions on Vehicular Technology**, [S.l.], v. 70, n. 2, p. 1941–1945, 2021. DOI: 10.1109/TVT.2021.3055040.

31 3GPP. **Moderator summary for multi-beam enhancement**: EVM. Technical discussion. [S.l.], 2020.

32 GIRNYK, M. A.; PETERSSON, S. O. A simple cell-specific beamforming technique for multi-antenna wireless communications. *In*: 2020 IEEE WIRELESS COMMUNICATIONS AND NETWORKING CONFERENCE (WCNC), 2020, Seoul. **Proceedings** [. . .]. New York: IEEE, 2020. p. 1–4. DOI: 10.1109/WCNC45663.2020.9120705.

33 IKUNO, J. C.; WRULICH, M.; RUPP, M. System level simulation of LTE networks. *In*: 2010 IEEE 71st VEHICULAR TECHNOLOGY CONFERENCE, 2010, Taipei. **Proceedings** [. . .]. New York: IEEE, 2010. p. 1–5. DOI: 10.1109/VETECS.2010.5494007.

34 _____. **TS 36.213**: Universal Terrestrial Radio Access (E-UTRA); physical layer procedures. Technical specification. [S.l.], 2009.